Geochemistry, Geophysics, Geosystems®

WISTFUL: Whole-Rock Interpretative Seismic Toolbox for Ultramafic Lithologies

William J. Shinevar[1,2] 📧, **Oliver Jagoutz[3]**, and **Mark D. Behn[4]** 📧

[1]MIT/WHOI Joint Program in Oceanography/Applied Ocean Engineering, Cambridge, MA, USA, [2]Now at University of Colorado Boulder, Boulder, CO, USA, [3]Massachusetts Institute of Technology, Cambridge, MA, USA, [4]Boston College, Chestnut Hill, MA, USA

Abstract To quantitatively convert upper mantle seismic wave speeds measured into temperature, density, composition, and corresponding and uncertainty, we introduce the **W**hole-rock **I**nterpretative **S**eismic **T**oolbox **F**or **U**ltramafic **L**ithologies (WISTFUL). WISTFUL is underpinned by a database of 4,485 ultramafic whole-rock compositions, their calculated mineral modes, elastic moduli, and seismic wave speeds over a range of pressure (*P*) and temperature (*T*) (*P* = 0.5–6 GPa, *T* = 200–1,600°C) using the Gibbs free energy minimization routine Perple_X. These data are interpreted with a toolbox of MATLAB® functions, scripts, and three general user interfaces: *WISTFUL_relations*, which plots relationships between calculated parameters and/or composition; *WISTFUL_geotherms*, which calculates seismic wave speeds along geotherms; and *WISTFUL_inversion*, which inverts seismic wave speeds for best-fit temperature, composition, and density. To evaluate our methodology and quantify the forward calculation error, we estimate two dominant sources of uncertainty: (a) the predicted mineral modes and compositions, and (b) the elastic properties and mixing equations. To constrain the first source of uncertainty, we compiled 122 well-studied ultramafic xenoliths with known whole-rock compositions, mineral modes, and estimated *P-T* conditions. We compared the observed mineral modes with modes predicted using five different thermodynamic solid solution models. The Holland et al. (2018, https://doi.org/10.1093/petrology/egy048) solution models best reproduce phase assemblages (~12 vol. % phase root-mean-square error [RMSE]) and estimated wave speeds. To assess the second source of uncertainty, we compared wave speed measurements of 40 ultramafic rocks with calculated wave speeds, finding excellent agreement (V_p RMSE = 0.11 km/s). WISTFUL easily analyzes seismic datasets, integrates into modeling, and acts as an educational tool.

1. Introduction

The upper mantle displays significant variations in seismic wave speeds (e.g., Auer et al., 2014; Golos et al., 2020; Priestley & McKenzie, 2013; Ritsema et al., 2011; Shen & Ritzwoller, 2016). Studies have used seismic wave speed as a proxy to constrain mantle temperature, density, and composition (e.g., Goes & van der Lee, 2002; Jordan, 1979; Lee, 2003; Schutt & Lesher, 2006) as to first order, seismic wave speeds are controlled by the mineral assemblage, pressure (*P*), temperature (*T*), as well as the presence of fluids and/or melt (e.g., Birch, 1960; Christensen, 1966; Hammond & Humphreys, 2000; Stixrude & Lithgow-Bertelloni, 2005). However, quantitative constraints on how wave speeds relate to mantle temperature, composition, and density variations in Earth's mantle are complex as the equilibrium mineral assemblage will depend not only on *P* and *T*, but also whole-rock composition and oxygen fugacity (e.g., Green & Ringwood, 1970; Holland et al., 2018; Stixrude & Lithgow-Bertelloni, 2011). Furthermore, anelastic reduction in shear modulus becomes significant at high temperatures (>800°C), further complicating the relationship between wave speeds and composition. Anelasticity is in turn controlled by *P*, *T*, grain size, wave frequency, and oxidation state (e.g., Cline et al., 2018; Faul & Jackson, 2015b; Karato, 1993). Because mantle wave speeds are affected by these parameters, there is a need to develop methodologies to quantitatively convert upper mantle seismic velocities into temperature, composition, and densities along with an estimate of uncertainty.

Here we present WISTFUL (**W**hole-rock **I**nterpretative **S**eismic **T**oolbox for **U**ltramafic **L**ithologies), a toolbox to quantitatively determine the best-fit temperature, composition, and density from mantle seismic wave speeds along with the associated uncertainties (Figure 1). WISTFUL utilizes a set of MATLAB® functions to compare mantle wave speeds, provided by the user, with a database of calculated wave speeds to find the best-fit temperature, composition, and density for a given pressure and anelasticity correction. Anharmonic seismic wave speeds

WISTFUL Workflow:

Perple_X (Connolly, 2009)   Literature + implicit elastic moduli incorporating anelasticity
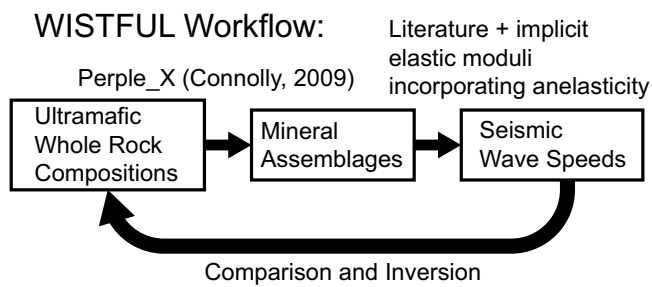

Figure 1. Schematic diagram illustrating the workflow implemented in WISTFUL.

are calculated for a database of 4,485 ultramafic whole-rock compositions at variable *P-T* conditions (200–1,600°C, 0.5–6 GPa). We use Perple_X (Connolly, 2009), the Holland and Powell (2011) thermodynamic database, and the thermodynamic solution models of Holland et al. (2018), which we find to best reproduce xenolith mineral assemblage (Section 3.2), to calculate the thermodynamically stable anhydrous mineral assemblages. We updated the database of elastic moduli in Perple_X to determine the seismic wave speed for each composition. Users can choose between two implementations of anelasticity corrections (Behn et al., 2009 or Jackson & Faul, 2010).

WISTFUL contains three MATLAB® general user interfaces (GUIs) and companion functions. The first GUI (*WISTFUL_relations*) plots relationships between parameters like the calculated elastic moduli, composition, and density. The second GUI (*WISTFUL_geotherm*) plots seismic wave speeds along various geotherms. The third GUI (*WISTFUL_inversion*) inverts for the best-fit temperature, composition, and density and visualizes the results.

The first part of this technical report describes previous work on the interpretation of seismic wave speed with respect to composition and temperature. The second part constrains uncertainties inherent to the forward calculation of seismic wave speeds from whole-rock compositions in order to evaluate the robustness of our methodology. The final part describes the data set behind WISTFUL and the MATLAB® functions and GUIs. The toolbox is provided via a supplement and is available online (github.com/wshinevar/WISTFUL, https://doi.org/10.5281/zenodo.5815695).

2. Previous Work

Classically, seismic wave speeds variations have been interpreted in terms of temperature and/or composition by comparison to laboratory measurements or calculated seismic wave speeds. Early work focused on understanding which rock-types produced wave speeds similar to observations (Birch, 1960; Christensen, 1966). More recent studies focused on compiling rock types and/or regional samples to link wave speeds directly to composition (Kelemen & Holbrook, 1995; Kern et al., 1996; Miller & Christensen, 1994). Other studies have analyzed mantle wave speeds using elastic parameters estimated from experiments to determine mantle temperatures (Cammarano et al., 2003; Goes & van der Lee, 2002; Goes et al., 2000). These approaches are limited by the existing laboratory measurements of seismic wave speed, which cover only a subset of known rock compositions. In addition, laboratory measurements of seismic wave speed for rock samples can be influenced by secondary low temperature alteration, which may not be present at high temperature in the lower crust and mantle (Gao et al., 2000; Rudnick & Fountain, 1995).

An alternative approach is to calculate seismic wave speeds by averaging the elastic moduli of individual minerals that constitute a rock in their appropriate proportions. Jordan (1979) calculated the modal assemblages and elastic properties of ultramafic rocks using major-element compositions of garnet lherzolites utilizing mineral norms, mineral partition coefficients, and mineral elastic properties to investigate the relationship between density, elastic properties, and mantle compositions. Duffy and Anderson (1989) compared mantle seismic profiles with mineral elastic parameters to constrain mantle mineral assemblage. Fountain and Christensen (1989) compiled seismic wave speed measurements of minerals and rocks together with xenolith observations to further constrain crustal and mantle compositions beneath the continental United States. More recent studies compiled laboratory measurements of mineral elastic moduli to calculate seismic wave speeds from a given mineral assemblage (Abers & Hacker, 2016; Hacker & Abers, 2004; Hacker, Abers, & Peacock, 2003). Other studies have calculated the physical properties of xenoliths and/or ultramafic rocks to better understand compositional effects on elastic properties (Afonso et al., 2010; Lee, 2003; Schutt & Lesher, 2006; Schutt & Lesher, 2010) and mantle anisotropy (Baptiste et al., 2012; Tommasi et al., 2004, 2008). A limitation to mineral averaging is that the input or observed mineral assemblages are not necessarily in thermodynamic equilibrium at all *P-T* conditions, potentially leading to misinterpretation of seismic wave speeds.

One solution to this limitation is to use thermodynamic modeling to predict the equilibrium mineral assemblage for a given bulk rock composition over a range of *P-T* conditions. The seismic wave speed for each mineral

assemblage is then calculated over the *P-T* range, accounting for wave speed changes due to variations in mineral composition and phase transitions (Helffrich et al., 1989; Sobolev & Babeyko, 1989, 1994). Sobolev et al. (1996, 1997) built upon this methodology by incorporating the effects of anelasticity and partial melt to interpret the mantle seismic wave speeds beneath the Massif Central, France. The combination of thermodynamic modeling in conjunction with laboratory-constrained mineral elastic moduli and densities has been used to interpret continental lower crust (e.g., Behn & Kelemen, 2003; Diaferia & Cammarano, 2017; Sammon et al., 2020), arc lower crust (e.g., Behn & Kelemen, 2006; Jagoutz & Behn, 2013), the mantle wedge at subduction zones (Hacker, Abers, & Peacock, 2003; Hacker, Peacock, et al., 2003), lunar mantle (Kuskov, Kronrod, Prokofyev, & Pavlenkova, 2014; Kuskov, Oleg, Kronrod, & Kronrod, 2014), cratonic lithospheric mantle (Kuskov et al., 2006; Kuskov, Kronrod, Prokofyev, & Pavlenkova, 2014; Kuskov, Oleg, Kronrod, & Kronrod, 2014), and continental geotherms and Moho temperatures (e.g., Diaferia et al., 2019; Schutt et al., 2018). To address the potential influence of sampling bias in compositional-wave speed relations, Behn and Kelemen (2003) applied thermodynamic modeling and compiled elastic moduli for a synthetic database intended to span the full compositional space of anhydrous igneous and meta-igneous rocks. The uncertainties in many thermodynamic models are difficult to constrain, with few studies comparing observed with predicted mineral assemblages or investigating how these uncertainties propagate into geophysical parameters such as wave speed and density (e.g., Afonso, Fullea, Griffin, et al., 2013; Behn & Kelemen, 2003; Connolly & Khan, 2016; Stixrude & Lithgow-Bertelloni, 2005).

With increasing computational resources, recent work has incorporated other geophysical measurements, including topography and gravity, to better constrain the composition and/or density of the mantle during seismic inversions (Kaban et al., 2014; Perry et al., 2003; Simmons et al., 2009, 2010). Other authors have utilized thermodynamic calculations of mantle compositions in the seismic tomographic inversion to estimate mantle composition and temperature (Khan et al., 2011; Zunino et al., 2016). Similarly, many authors (e.g., Afonso, Fullea, Griffin, et al., 2013; Afonso, Fullea, Yang, et al., 2013; Afonso et al., 2016; Fullea et al., 2021; Jones et al., 2017; Shan et al., 2021; Tunini et al., 2014, 2016) have utilized probabilistic joint inversions built on the forward-modeling of LitMOD (Afonso et al., 2008; Fullea et al., 2009; Kumar et al., 2020) to integrate seismic delay times, gravity data, geoid height, topography, and/or heat flow to decipher the compositional and thermal state of the crust and mantle. Further work has added long wavelength resistivity measurements to inversions in order to estimate the mantle water content (Khan, 2016; Khan et al., 2015).

To improve on previous studies concerning the interpretation of seismic wave speed, WISTFUL aims to investigate the uncertainty in the forward calculation of ultramafic seismic wave speeds and to create a methodology for quantitatively converting mantle seismic wave speeds into best-fit temperature, composition, and density.

3. Uncertainty in Seismic Wave Speed Forward Calculations

In this section, we first discuss how seismic wave speed is calculated from whole-rock composition (Section 3.1) in order to illustrate the uncertainties inherent to calculating seismic wave speeds from whole-rock compositions using thermodynamic models. Specifically, we investigate two sources of uncertainty: (a) uncertainty due to the misprediction of mineral assemblage and composition (Section 3.2), and (b) uncertainty due to uncertainties in the elastic property measurements and mixing equations (Section 3.3). We estimate the first uncertainty by comparing thermodynamic calculations of mineral assemblages and wave speeds to a compilation of xenoliths with wave speeds calculated directly from the reported mineral assemblages and compositions. In this comparison, the wave speed difference is due to the misprediction of mineral composition and modes. To constrain the second uncertainty, we compare ultrasonic seismic wave speed measurements of ultramafic rocks to calculated wave speeds for the same mineral modes and compositions using endmember moduli and mixing theory. In this comparison the *P-T* and mineral assemblage are constrained, and thus any discrepancies in wave speeds are due to uncertainty in the elastic moduli and mixing theory.

All thermodynamic calculations in WISTFUL were conducted using the Gibbs-free-energy minimization program Perple_X version 6.9.1 (Connolly, 2009), downloaded on 15 April 2021. Perple_X calculates stable mineral assemblages and compositions based on a chosen set of thermodynamic solution models and whole-rock composition for each rock sample. From the mineral assemblages, Perple_X calculates aggregate elastic moduli, density, and seismic wave speed as described below. One benefit of Perple_X is that a variety of thermodynamic databases and mineral solution models from different groups can be used. Other free energy minimization programs
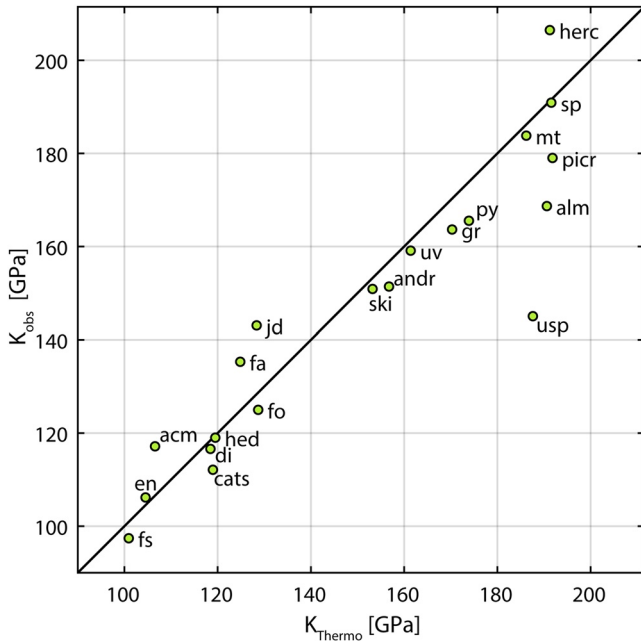
Figure 2. Experimental bulk moduli (K_{obs}) plotted against thermodynamically-derived bulk moduli (K_{Thermo}) for mantle mineral phase endmembers with experimental data at 500°C and 1 GPa using the Holland and Powell (2011) database. Abbreviations: acm, acmite; alm, almandine; andr, andradite; cats, Ca-tschermak; di, diopside; en, enstatite; fa, fayalite; fo, forsterite; gr, grossular; hed, hedenbergite; herc, hercynite; jd, jadeite; mgcr, magnesiochromite; mt, magnetite; py, pyrope; ski, skiagite; sp, spinel; usp, ulvospinel; uv, uvarovite.

like THERMOCALC (Holland & Powell, 1998; Powell & Holland, 1994), Theriak-Domino (De Capitani & Petrakakis, 2010), or HeFESTo (Stixrude & Lithgow-Bertelloni, 2011) do not allow such an easy comparison of solution models. Another advantage is that the elastic moduli data in the thermodynamic database can be easily updated to incorporate new measurements. The integration of thermodynamic calculations and moduli estimation in a single algorithm allows for a simple, integrated workflow.

3.1. Calculating Seismic Wave Speeds

To calculate the elastic moduli of a mineral solid-solution, Perple_X uses a Reuss average (Reuss, 1928) weighted by molar volume of the respective mineral endmembers:

$$G^{mineral} = \left(\left[\frac{1}{V^{mineral}} \right] \sum \frac{X^{endmember} V^{endmember}}{G^{endmember}} \right)^{-1}, \qquad (1)$$

where $V^{endmember}$ and $X^{endmember}$ are the molar volume and molar fraction of the endmember, respectively. $V^{mineral}$ is the molar volume for the mineral solid solution, and G is the shear modulus. Aggregate rock elastic moduli are then calculated using a Voigt-Reuss-Hill average (Hill, 1952):

$$G^{rock} = \frac{1}{2} \left(\sum F^{mineral} G^{mineral} + \frac{1}{\sum F^{mineral}/G^{mineral}} \right), \qquad (2)$$

where $F^{mineral}$ is the volume fraction of each mineral. An equivalent expression can be written for the adiabatic bulk modulus (K) by replacing the mineral and endmember shear moduli with bulk moduli. The seismic wave speeds for the aggregate are then calculated as:

$$V_s = \sqrt{\frac{G^{rock}}{\rho^{rock}}}, \qquad (3)$$

and

$$V_p = \sqrt{\frac{K^{rock} + \frac{4}{3} G^{rock}}{\rho^{rock}}} \qquad (4)$$

where V_s is the shear wave speed, V_p is the primary wave speed, ρ^{rock} is the bulk rock density, and K^{rock} is the adiabatic bulk moduli for the aggregate rock.

Perple_X allows two options for calculating mineral elastic moduli. The first calculates the bulk modulus of each mineral endmember from the Gibbs energy equation. In this approach, the shear modulus is calculated from the bulk moduli using a given Poisson's ratio. In the second approach, Perple_X calculates the elastic moduli based on elastic moduli derived from experimental observations using different formulations for different solution models (as described in the next paragraph). Overall, there is good agreement between the experimental and calculated bulk moduli (Figure 2) with a root-mean-square error (RMSE) on bulk moduli of 8.5 GPa (~6% assuming an average bulk modulus of 150 GPa.). In general, we find that most thermodynamically derived bulk moduli are slightly higher than the experimental observations, suggesting that thermodynamically calculated seismic wave speeds are likely overpredictions. Further, the calculated bulk moduli of a few specific minerals are greatly underpredicted (e.g., jadeite by 15 GPa, 10% of experimental value) or overpredicted (e.g., ulvospinel by 42 GPa, 29% of experimental value). This illustrates that when available, it is preferential to use experimental moduli to minimize error in calculating seismic wave speeds.

For the calculations in WISTFUL, we utilize experimentally constrained elastic moduli when available (updated from Abers and Hacker (2016) database; see Table 1 for further additions to the database). Perple_X uses linear

Table 1
Newly Input Elastic Moduli and Derivatives Used in the Seismic Wave Speed Calculations

Mineral endmember	Chemical formula	Ambient adiabatic bulk moduli, K (GPa)	Bulk pressure derivative, K'	Bulk temperature derivative, K_T (GPa/K)	Ambient shear moduli, G (GPa)	Shear pressure derivative, G'	Shear temperature derivative, G_T (GPa/K)
Monticellite	$CaMgSiO_4$	106[5]	3.9[4]	−0.014[1]	55.2[5]	2.03[3]	−0.073[3]
Spessartine	$Mn_3Al_2Si_3O_{12}$	191.5[6]	4.1[6]	−0.020[1]	96.3[7]	2.1[3]	−0.010[3]
Andradite	$Ca_3Fe_2Si_3O_{12}$	154.5[8]	4.7[8]	−0.016[9]	89.7[8]	1.25[8]	−0.009[3]
Skiagite	$Fe_5Si_3O_{12}$	157.4[10]	6.7[10]	−0.0278[1]	76.4[11]	3.27[3]	−0.0135[3]
Uvarovite	$Ca_3Cr_2Si_3O_{12}$	163[12]	4.4[12]	−0.017[12]	89.9[13]	1.8[13]	−0.010[3]
Knorringite	$Mg_3Cr_2Si_3O_{12}$	163[2]	4.4[2]	−0.017[2]	89.9[2]	1.8[2]	−0.010[2]
K-jadeite	$KAlSi_2O_6$	147.4[1]	4.9[1]	−0.017[1]	85[2]	1.9[2]	−0.0059[2]
Acmite	$NaFeSi_2O_6$	119[20]	4.1[20]	−0.013[1]	85[2]	1.9[2]	−0.0059[2]
Kosmochlor	$NaCrSi_2O_6$	124[19]	3.6[19]	−0.010[1]	85[2]	1.9[2]	−0.0059[2]
Periclase	MgO	162.8[14]	3.94[14]	−0.025[14]	130.3[14]	2.17[14]	−.02[14]
Ulvospinel	$TiOFe_2O_5$	151[15]	3.8[15]	−0.0215[1]	26[16]	0.654[3]	−0.004[3]
Magnesiochromite	$MgCr_2O_4$	185[17]	5.7[17]	−0.0243[1]	130[18]	4.0[3]	−0.0171[3]
Corundum	Al_2O_3	254.8[21]	4.06[21]	−0.0202[21]	168[21]	1.44[21]	−0.0227[21]
Qandilite	Mg_2TiO_4	152[22]	3.91[1]	−0.0129[1]	77[22]	1.98[3]	−0.0065[3]

Note. Notes and references: (1) Derived from thermodynamic properties, (2) Taken from nearest endmember, (3) Fit to maintain ambient *P-T* Poisson's ratio, (4) Sharp et al. (1987), (5) Peercy and Bass (1990), (6) Zhang et al. (1999) (7) Bass (1989), (8) Jiang et al. (2004), (9) Pavese et al. (2001), (10) Woodland et al. (1999), (11) Vasiukov et al. (2018), (12) Gréaux and Yamada (2019), (13) Wang and Ji (2001), (14) Fan et al. (2019), (15) Xiong et al. (2015) (16) Syono et al. (1971) (17) Nestola et al. (2014) (18) estimated in Matsukage et al. (2010), (19) Posner et al. (2014), (20) Xu et al. (2017), (21) Wang and Wu (2018), (22) Liebermann et al. (1977). All isothermal bulk moduli and derivative measurements were converted to adiabatic moduli and derivatives as described in Section 3.1.

temperature and pressure derivatives when extrapolating experimental moduli for solution model sets using the Holland and Powell (2011) databases. Perple_X calculates elastic moduli using Mie-Grüneisen formulations from Stixrude and Lithgow-Bertelloni (2005) assuming the Stixrude and Lithgow-Bertelloni (2011) solution models. The Abers and Hacker (2016) methodology calculates the temperature dependence of the elastic moduli using Grüneisen parameters and the pressure dependence from finite-strain theory based on Bina and Helffrich (1992). To convert the compiled parameters from Abers and Hacker (2016) to linear temperature and pressure derivatives used in the Holland and Powell (2011) databases, we fit linear derivatives from the calculated mineral endmember moduli over 100–800°C and 0.1–2.0 GPa.

When no experimental data exist for a specific mineral endmember, the adiabatic bulk modulus and its pressure and temperature derivatives were derived from the Gibbs free energy (cf. Bina & Helffrich, 1992) over a range of 200–1,400°C and 0.1–6 GPa using the Perple_X routine *frendly*. These results were fit to an explicit linear form using MATLAB *cftool*. The only exception to this method was the garnet endmember knorringite ($Mg_3Cr_2[SiO_4]_3$), for which we assumed the same observed bulk and shear modulus as garnet endmember uvarovite ($Ca_3Cr_2[SiO_4]_3$) (Table 1) under the assumption that chromium garnets have similar elastic moduli. For mineral endmembers with an experimentally constrained bulk modulus at ambient conditions exist, but no temperature and/or pressure derivatives, we utilize the observed bulk modulus along with derivatives fit as described above. If the literature reported isothermal rather than adiabatic bulk moduli or derivatives, the data was converted into adiabatic bulk moduli following the assumptions made in Abers and Hacker (2016).

Unlike bulk moduli, shear moduli cannot be thermodynamically derived. If no shear moduli data are provided, Perple_X calculates the shear moduli assuming a constant Poisson's ratio (default 0.35) for all minerals. However, Poisson's ratios for mantle mineral endmembers vary from 0.20 to 0.35 at room temperature and pressure and can change up to ~8% between ambient conditions and 800°C, 1 GPa based on our updated moduli database. Thus, the assumption of a constant Poisson's ratio increases the uncertainty on these calculations. To minimize

this error, we utilize all available experimental shear modulus and derivatives. If experimental shear modulus data at ambient conditions exist, but no constraint is available for pressure and/or temperature derivatives, we estimate these derivatives from the bulk modulus derivatives while maintaining the Poisson's ratio calculated at ambient conditions. If no shear modulus data exist for an endmember composition, we utilize the shear modulus data of the closest ionic endmember (Table 1). This approach gives our best estimate of that endmember mineral's Poisson's ratio.

3.2. Thermodynamic Model Uncertainty

To assess the uncertainty in seismic wave speed due to errors in the thermodynamic modeling, Afonso, Fullea, Griffin, et al. (2013) compared calculated to point-counted mineral modes of 10 garnet peridotite xenoliths (six lherzolites, four harzburgites) at the *P-T* conditions constrained from mineral thermobarometers. The thermodynamically calculated mineral modes agree well with point counting estimates and the remaining modal variations did not greatly affect the predicted wave speeds. However, a limitation of comparing thermodynamic models with xenoliths is the small data set of samples that have detailed laboratory measurements (e.g., modal assemblage and *P-T* estimates). Further, there is no reliable spinel-peridotite mineral barometer, so previous comparisons were limited to garnet-bearing xenoliths and contained no spinel-bearing peridotites or pyroxenites.

Fortunately, with advances in electron-backscatter diffraction (EBSD), more peridotite and pyroxenite xenoliths have been studied in detail with modal assemblage estimates. Utilizing these data along with mineral assemblages constrained by least-squares-regression of mineral and bulk compositions, we (a) expanded the xenolith database of Afonso, Fullea, Yang, et al. (2013) to include samples with a larger compositional and *P-T* range, including spinel-garnet peridotites, spinel peridotites with geotherm-based barometry, and pyroxenites; and (b) explored multiple solution models (and oxygen states for solution models that utilize Fe_2O_3) to determine the most reliable solution model(s). The benefit of comparing thermodynamically predicted mineral assemblages with xenoliths, rather than with mineral assemblages of petrologic experiments, is that thermodynamic models are calibrated with those petrologic experiments. Therefore, thermodynamic model validations obtained through comparison to petrologic experiments are circular if the same experiments were used to calibrate the model.

We investigate the uncertainty in five published sets of solution models for the dominant mantle minerals: olivine, orthopyroxene, clinopyroxene, plagioclase, spinel and garnet (Table 2). The majority of these solution models are anhydrous, and ignore the thermodynamic influence of H_2O, which we do not consider here. The solution models range in complexity with newer solution models integrating more major elements. For example, Jennings and Holland (2015) incorporates Cr_2O_3 into clinopyroxene, orthopyroxene, spinel, and garnet solution models. Other newer solution models have been calibrated on broader compositional ranges (e.g., Holland et al., 2018 is calibrated to model both granitic and ultramafic melting). Our aim in choosing these model sets is to test all major solution models that have been calibrated for ultramafic compositions. Melt solution models were excluded from the calculations. No minimum equilibration temperature cutoff (i.e., the temperature at which equilibration ceases) was used for the comparison calculations. Assuming an 800°C temperature cutoff (i.e., using the phases calculated at 800°C at all temperatures <800°C, but calculating the physical properties at the queried temperature), does not change the results.

We compiled 122 xenoliths with the following attributes: (a) available *P-T* estimates, (b) less than 2 vol. % hydrous phase (e.g., phlogopite or amphibole), (c) reported chemical compositions for all minerals, (d) reported major-element bulk rock composition that are either measured or calculated from mineral compositions and modes, and (e) a mineral modal assemblage that is either measured via electron-backscatter diffraction (EBSD) or calculated by least-squares regression from bulk rock and mineral compositions (data available in Table S1 in Supporting Information S1). Xenolith samples were compiled from Lee and Rudnick (1999), Falus et al. (2008), Ionov et al. (2010), Baptiste et al. (2012), Tommasi and Ishikawa (2014), and Demouchy et al. (2015). If a whole-rock composition was calculated from the mineral modes and compositions, we used the following densities to convert vol. % to wt. % for the major minerals based on Abers and Hacker (2016): olivine 3,340 kg m⁻³, orthopyroxene 3,280 kg m⁻³, clinopyroxene 3,310 kg m⁻³, spinel 3,850 kg m⁻³, and garnet 3,800 kg m⁻³. Ninety-two (75%) of the xenoliths are peridotites (>40 vol. % olivine normalized to olivine-orthopyroxene-clinopyroxene); the remaining 30 (25%) are pyroxenites (<40 vol. % olivine). None of these peridotites contain plagioclase; therefore, our data set provides no constraint on the shallowest part of the mantle (~20 km depth, Borghini et al., 2010). Most of the xenoliths come from continental regimes with the exception of oceanic and plume

Table 2
List of Solution Models Sets Used for Xenolith Comparisons

Solution model set	Holland and Powell (1998)	Cr Holland and Powell	Stixrude and Lithgow-Bertelloni (2011)	Jennings and Holland (2015)	Holland et al. (2018)
Elemental System:	Na_2O-CaO-FeO-MgO-Al_2O_3-SiO_2-Fe_2O_3 (NCFMASO)	Na_2O-CaO-FeO-MgO-Al_2O_3-SiO_2-Fe_2O_3-Cr_2O_3 (NCFMASOCr)	Na_2O-CaO-FeO-MgO-Al_2O_3-SiO_2 (NCFMAS)	Na_2O-CaO-FeO-MgO-Al_2O_3-SiO_2-Fe_2O_3-Cr_2O_3 (NCFMASOCr)	K_2O-Na_2O-CaO-FeO-MgO-Al_2O_3-SiO_2-H_2O-TiO_2-Fe_2O_3-Cr_2O_3 (KNCFMASTOCr)
Olivine	O(HP)	O(HP) (Holland & Powell, 1998)	O	O(JH)	O(HGP)
Orthopyroxene	Opx(HP) (Powell & Holland, 1999)	CrOpx(HP) (Powell & Holland, 1999)	Opx	Opx(JH)	Opx(HGP)
Clinopyroxene	Cpx(HP) (Holland & Powell, 1996)	Cpx(HP) (Holland & Powell, 1996)	Cpx	Cpx(JH)	Cpx(HGP)
Garnet	Gt(HP)	CrGt (Malaspina et al., 2009; Ziberna et al., 2013)	Gt_maj	Grt(JH)	Gt(HGP)
Spinel	Sp(HP)	CrSp (Klemme et al., 2009)	Sp	Sp(JH)	Sp(HGP)
Plagioclase	Pl(I1,HP) (Holland & Powell, 2003)	Pl(I1,HP) (Holland & Powell, 2003)	Pl	Pl(JH)	Pl(I1,HP) (Holland & Powell, 2003)

Note. References are given for the solution models not taken from the set reference. The Holland and Powell (2011) thermodynamic database was used for all the calculations with the exception of the Stixrude and Lithgow-Bertelloni (2011). We used 0 wt. % TiO_2, K_2O, and H_2O for our calculations using Holland et al. (2018) as using K_2O and TiO_2 when available increased phase and wave speed errors.

influenced mantle xenoliths from the Ontong Java plateau (Tommasi & Ishikawa, 2014). *P-T* estimates for these xenoliths cover pressures from 1.2 to 6.8 GPa and temperatures of 656–1,414°C.

For each xenolith sample, there exists errors in the mineral modes estimates, whole-rock compositions, mineral compositions, and oxidation states. Most thermobarometric estimates report 2σ errors of 4–6 kbar and 100°C (Brey & Köhler, 1990; Nickel & Green, 1985). Furthermore, the xenolith assemblages may not record the same equilibration conditions as the mineral thermobarometry. While point counting errors should be minimal, the mineral assemblages in a thin section may not represent the entire equilibrium system due to the small scale of the thin section. Similarly, measured whole-rock compositions may not reflect the equilibrium whole-rock composition for a sample. Conversely, if the whole-rock composition and/or modal assemblage is calculated from the mineral compositions, variability in the mineral compositions will produce errors. This is especially true for lower concentration elements, as phase equilibria is often sensitive to variations of lower concentration elements, for example, Fe_2O_3 and Cr_2O_3, which can drastically increase the spinel stability field (Klemme, 2004). Further analysis is needed to constrain the effects of these errors on our validation.

Oxidation state can also impact the stable mineral assemblage for ultramafic compositions, as more oxidized compositions will contain more ferric iron bearing phases like pyroxene, spinel, and garnet. Direct measurements on primitive peridotites suggests mantle $Fe^{3+}/\sum Fe$ of 3.5 mol. %, but can vary between 1 and 6 mol. % (Canil et al., 1994, gray box Figure 3) and varies with the relative depletion of the peridotite. This estimate (>3 mol. %) is supported by measurements of $Fe^{3+}/\sum Fe$ contents in primary MORB (Cottrell & Kelley, 2011). Mineral assemblages and elastic seismic wave speeds were calculated for each xenolith at the estimated *P-T* conditions using each set of solution models over a range of oxidation states (0–10 mol. % $Fe^{3+}/\sum Fe$, colored lines, Figure 3). In addition, a set of calculations was performed where the mol. % $Fe^{3+}/\sum Fe$ was constrained for each sample by the observationally-derived equation (Canil et al., 1994):

$$\frac{Fe^{3+}}{\sum Fe} = 14.7 - 0.3\,MgO, \tag{5}$$

where MgO is the bulk rock MgO content in wt. % (triangles, Figure 3). The Stixrude and Lithgow-Bertelloni (2011) (SLB, green square, Figure 3) solution models do not incorporate ferric iron.
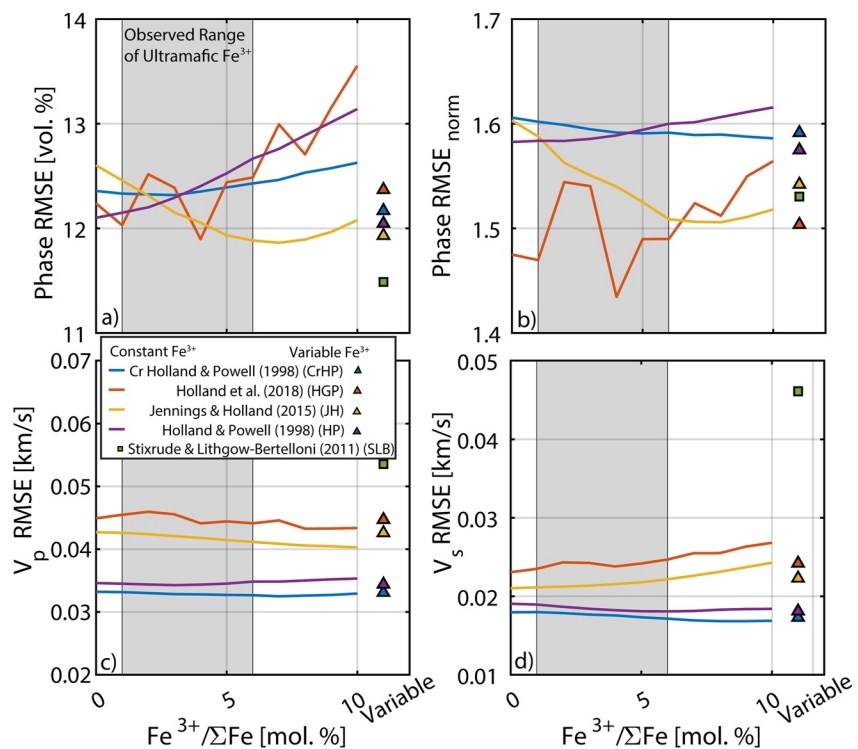
Figure 3. Root-mean-square error (RMSE) for the mineral phase and seismic wave speed calculated for all five solution models relative to the xenolith database as a function of $Fe^{3+}/\sum Fe$. Gray box shows the range of observed $Fe^{3+}/\sum Fe$ in ultramafic rocks (Canil et al., 1994). RMSE for the Stixrude and Lithgow-Bertelloni (2011) model is constant because it does not include Fe_2O_3 in its solution model.

To identify the set of solution models that best match the observed mineral assemblage, the RMSE was calculated for each mineral mode (olivine, orthopyroxene, clinopyroxene, garnet, and spinel) and summed for each xenolith. The summed phase RMSE was averaged over all xenoliths to estimate the total phase error (Figure 3a, dispersion shown in Figure S1a in Supporting Information S1). Overall, we find that the SLB solution models provides the lowest phase RMSE (11.5 vol. %) (green square, Figure 3a), followed by the Jennings and Holland (2015) solution models at variable $Fe^{3+}/\sum Fe$ and 6–7 mol. % $Fe^{3+}/\sum Fe$ (11.9 vol. %) (JH, orange line and triangle, Figure 3) and the Holland et al. (2018) solution models at 4 mol. % $Fe^{3+}/\sum Fe$ (11.9 vol. %) (HGP, red line). Although the SLB database produces slightly lower phase RMSE, the SLB solution models simplify certain phase transitions like the garnet-spinel transition due to the lack of Fe_2O_3 and Cr_2O_3, which allow for higher-pressure spinel stability as well as spinel-garnet co-stability (Klemme, 2004). This simplification may cause misinterpretation at shallow mantle conditions. Furthermore, a larger spinel stability field reduces the strength of relationship between V_p/V_s and Mg # at shallow depths (Afonso et al., 2010). Thus, accurately modeling the spinel stability field is important for inferring composition from seismic wave speed. Since the phase RMSE considers a 1 vol. % error in a minor phase equal to a 1 vol. % in a major phase, we also calculated a phase $RMSE_{norm}$, where each individual phase RMSE is normalized by the amount of that phase averaged over all samples (Figure 3b, dispersion shown in Figure S1b in Supporting Information S1). The HGP solutions models at 4 mol. % $Fe^{3+}/\sum Fe$ result in the lowest $RMSE_{norm}$ (1.43) due to the HGP models predicting spinel stability considerably better than all other models (Figure S6 in Supporting Information S1).

Figure 4 compares the predicted and observed mineral modes for the HGP solution models assuming 4 mol. % $Fe^{3+}/\sum Fe$. The HGP solution models predict olivine modes well (RMSE = 1.9 vol. %, $RMSE_{norm}$ = 0.03, mean error (ME, predicted-observed) = −0.78 vol. %) and orthopyroxene (RMSE = 3.5 vol. %, $RMSE_{norm}$ = 0.17, ME = −0.04 vol. %). A comparison of the predicted and observed mineral modes for all minerals and solution model sets is shown in Figures S2–S6 in Supporting Information S1. The HGP solution models tend to overpredict garnet (RMSE = 3.3 vol. %, $RMSE_{norm}$ = 0.33, ME = 3.0 vol. %) and underpredict clinopyroxene (RMSE = 2.7 vol. %, $RMSE_{norm}$ = 0.18, ME = −2.0 vol. %), especially in the pyroxenite xenoliths.
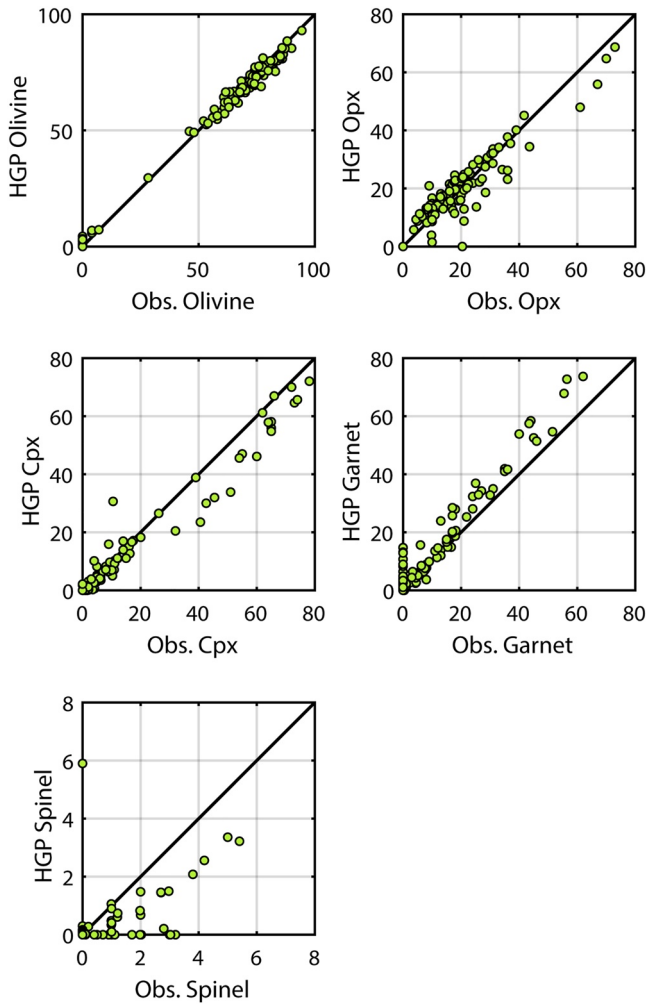
Figure 4. Mineral proportions for all xenoliths at their equilibrium conditions calculated using the Holland et al. (2018) solution models and 4 mol. %Fe$_2$O$_3$/FeO^T plotted against the observed mineral proportions. All values are given in vol. %.

While the HGP solution models do better than other models at predicting spinel, the HGP models often underpredict the spinel mode for spinel bearing peridotites, predicting no spinel for 20 of 45 spinel-bearing samples. 13 of these 20 samples also have no observed garnet, and thus have pressures estimated from geotherms and geothermometers. This implies the modal error could be due to over-estimation of equilibration pressure. The HGP solution models also predict spinel to be stable in nine xenoliths where no spinel was observed. Three of these samples have no garnet present, so part of this mismatch could also be due to error in the pressure estimates. Other discrepancies in the modal error could be due to xenoliths recording non-equilibrium conditions or uncertainties in low concentration elements like Fe$_2$O$_3$ and Cr$_2$O$_3$ are especially important for spinel-stability (Klemme, 2004). Due to the small volume amount of spinel stable in peridotites, error in the spinel modes does not strongly contribute to the phase RMSE, but contributes almost half of the RMSE$_{norm}$ (RMSE = 0.44 vol. %, RMSE$_{norm}$ = 0.67, ME = −0.33 vol. %).

To quantify how the modal assemblage and mineral composition uncertainty translates to anharmonic seismic wave speed uncertainty, we compare anharmonic seismic wave speeds calculated by Perple_X for each solution model with anharmonic seismic wave speeds calculated using known mineral mode assemblages and compositions for each xenolith at the equilibrium P-T conditions. Minerals were decomposed into endmember compositions following Wood and Banno (1973) and Holland et al. (2018). All Ni and Mn endmembers were considered to have the same elastic moduli as the Mg endmembers for these calculations when Ni and Mn were measured in the xenoliths with the exception of spessartine. Elastic parameters and densities were taken at the specified P-T conditions for each endmember mineral and then averaged as they would be in Perple_X (see Section 3.1).

From the predicted seismic wave speeds for each xenolith, we calculate an RMSE for wave speeds to estimate the deviation caused by the combination of the phase error and the mineral composition error (Figures 3c and 3d, dispersion shown in Figures S1c and S1d in Supporting Information S1). Oxidation state, while strongly controlling phase RMSE, does not strongly impact wave speed error. The Cr Holland and Powell (1998) (CrHP) and Holland and Powell (1998) (HP) models produces the lowest wave speed errors with 0.02 km/s in V$_s$ (Figures 3c, S7, and S8 in Supporting Information S1) and 0.03 km/s for V$_p$ (Figure 3d), equivalent to 0.5% and 0.4%

assuming a mantle V$_p$ and V$_s$ of 8.0 km/s and 4.5 km/s, respectively. The JH and HGP models produce slightly higher V$_p$ RMSE (0.04 km/s, 0.5%) and V$_s$ RMSE (0.02 km/s, 0.5%) (Figure 5 and S9 in Supporting Information S1). There is little systemic bias in the HGP errors with V$_p$ ME (0.02 km/s) and V$_s$ ME (0.01 km/s) (Figure S10 in Supporting Information S1). The SLB models produce a 0.05 km/s error in both V$_p$ and V$_s$ (0.6% and 1.1%, respectively). This uncertainty of ∼0.5% in the forward calculation of seismic wave speed is similar to the calculated bootstrap uncertainty (0.1–0.5%) at shallow depths (<200 km) in recent seismic models (Golos et al., 2020; Shen & Ritzwoller, 2016).

Overall, we prefer the HGP solution models at 4 mol. % Fe^{3+}/∑Fe to minimize phase RMSE and normalized phase RMSE, while predicting seismic wave speed only slightly more poorly than the CrHP and HP models (∼0.01 km/s in V$_p$ and V$_s$). We note that the largest errors for wave speed in the HGP model are in pyroxenites (Figure 5), likely due to HGP's overprediction of garnet in pyroxenite compositions (Figure 4). Further, the assumed 4 mol. % Fe3+/∑Fe agrees with available constraints on mantle oxidation state.
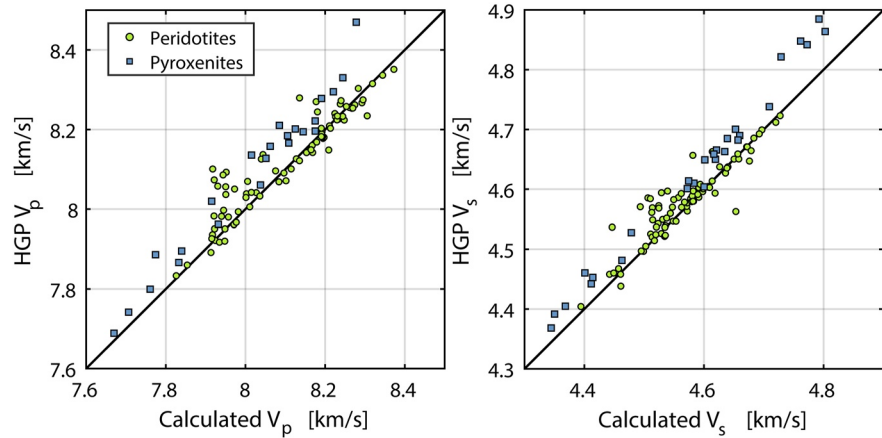
Figure 5. Seismic wave speeds for all xenoliths at their equilibrium conditions calculated using the Holland et al. (2018) solution models with 4 mol. % $Fe^{3+}/\sum Fe$ plotted against the seismic wave speeds calculated from the observed mineral modes and mineral compositions.

3.3. Mixing Theory and Moduli Uncertainty

To validate the mixing calculations and moduli for ultramafic minerals discussed in Section 3.1, we compiled multi-directional seismic wave speed measurements for 40 ultramafic rocks for which modal assemblages are reported (compiled in Table S2 in Supporting Information S1, Babuška, 1972; Birch, 1960, 1961; Christensen, 1966, 1974, 1978, 1979; Christensen & Ramananantoandro, 1971; Kono et al., 2004, 2009; Kroenke et al., 1976; Mao et al., 1970; O'Reilly et al., 1990; Peselnick & Nicolas, 1978; Prelicz, 2005; Ramana & Rao, 1974). We decompose the minerals into the mineral endmembers following Wood and Banno (1973) and Holland et al. (2018) and calculate the seismic wave speed following the same approach as Perple_X. In some studies (Birch, 1960, 1961; Christensen, 1966, 1974, 1978; Christensen & Ramananantoandro, 1971; Kroenke et al., 1976; Peselnick & Nicolas, 1978; Prelicz, 2005), orthopyroxene and/or clinopyroxene were present in the samples, yet both mineral compositions were not provided. When orthopyroxene is reported, but its chemical composition is not provided and no literature data exist, we calculate a theoretical orthopyroxene composition in equilibrium with the reported olivine composition. Here we assume orthopyroxene is purely enstatite-ferrosillite and use an olivine-orthopyroxene partition coefficient $K_D^{Ol-Opx} = Y_{Mg}^{Opx} Y_{Fe}^{Ol} / Y_{Mg}^{Ol} Y_{Fe}^{Opx} = 1.15$ based on experimental studies (von Seckendorff and O'Neill, 1993). Y_{Mg} and Y_{Fe} are the molar fraction of Mg or Fe in the respective superscript. Similarly, we calculate a theoretical clinopyroxene composition in equilibrium with either olivine or orthopyroxene compositions assuming clinopyroxene is purely diopside-hedenbergite and use an orthopyroxene-clinopyroxene partition coefficient $K_D^{Cpx-Opx} = Y_{Mg}^{Opx} Y_{Fe}^{Cpx} / Y_{Mg}^{Cpx} Y_{Fe}^{Opx} = 1$ in line with experiments and field observations at equilibration temperatures 1,000–1,200°C (Kretz, 1982; Mori & Green, 1978). Triaxial seismic wave speed measurements were averaged to obtain the isotropic wave speeds (18/40 samples). We compare our theoretical calculated wave speeds with the highest-pressure measurements (1 GPa for 32 of the 40 samples) to minimize the effects of cracks or porosity that are often present in natural samples.

There is an excellent agreement between the laboratory-derived wave speed data and wave speeds calculated using reported mineral assemblage and mineral endmember moduli (RMSE = 0.11 km/s) with a slight tendency for overprediction (ME = 0.05 km/s) (Figure 6). This misfit could be due to miscounting of mineral modes, experimental uncertainty in seismic wave speed measurements (often ~1% or ~0.08 km/s), uncertainty in the elastic moduli for each endmember, sample anisotropy, lower pressure (0.4–0.5 GPa)
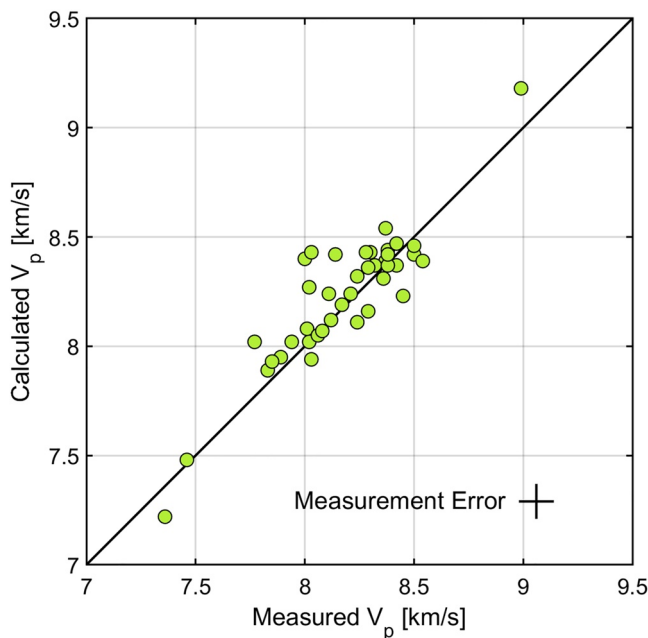

Figure 6. V_p calculated for ultramafic rocks from modal assemblage, modal composition, and predicted mineral moduli versus laboratory measured V_p. See Section 2 for details. Estimated measurement error in both directions shown in bottom right. Measurement error depicts 1% error in both direction.

Table 3
WISTFUL Databases, Functions, General User Interfaces (GUIs), and Scripts

Filename	Purpose
README.txt	A readme file with units and descriptions of all files in WISTFUL
Databases	
WISTFUL_compositions_clean.mat	Compositional database with latitude and longitude of samples
WISTFUL_densities_clean.mat	Database with densities
WISTFUL_parsed_modes_clean.mat	Database with mineral modes
WISTFUL_rockType.mat	Database file with rock type information
WISTFUL_speeds_moduli_clean.mat	Database with moduli and wave speeds
Functions	
behn2009Shear.m	Function to calculate Behn et al. (2009) anelasticity
creep10.m, J1anel.m, J1p.m, J2anel.m, J2p.m	Functions to calculate Jackson and Faul (2010) anelasticity written by Uli Faul
findClosestX.m	Function to find the closest X samples to a input seismic wave speed at a pressure and temperature range
fitPropertyClosestX.m	Function to find best fit property with output from findClosestX.m
fitPropertyNumWithin.m	Function to find best fit property with output from numWithinError.m
numWithinError.m	Function to find the number of samples within error from seismic data at a given pressure and temperature range
calculateWaveSpeedFiles.mlx	Live function to apply anelastic corrections to the database
GUIs	
WISTFUL_inversion.mlapp	Inversion GUI
WISTFUL_geotherm.mlapp	Geotherm Profile GUI
WISTFUL_relations.mlapp	Relations GUI
Example Scripts	
exampleNumWithin.m, exampleClosestX.m	Example scripts

experiments not fully closing pore space in line with larger discrepancies, and/or uncertainty on the exact compositions of each mineral for measurements that only report olivine composition. Altogether, we interpret this low error (∼1.4% assuming V_p = 8.0 km/s) as justification for our choice of the elastic moduli mixing approach described above and moduli data for ultramafic assemblages.

4. WISTFUL

With the methods, errors, and assumptions associated with calculating seismic wave speed using thermodynamic calculations and elastic moduli in mind, we now describe WISTFUL. We first discuss the composition database used for the seismic wave speed calculations, and second describe how to use the associated functions and GUIs. All database files, functions, and MATLAB® GUIs are listed in Table 3 and are available on github.com/wshinevar/WISTFUL or https://doi.org/10.5281/zenodo.5815695. To use the functions and GUIs, place the directory containing all .m code files and .mat database files in your MATLAB® search path or in your current directory. The code described here was tested using MATLAB® 2021a.

4.1. Compositional Database

Major element compositions for the ultramafic rocks used by WISTFUL were compiled by downloading all rocks labeled as peridotite, dunite, lherzolite, harzburgite, xenolith peridotite, pyroxenite, and wehrlite from the EarthChem (http://portal.earthchem.org/) and GEOROC (http://georoc.mpch-mainz.gwdg.de/georoc/) databases on 24 January 2019. Duplicate compositions were removed. To this data set we added whole-rock compositions from Beni Bousera Massif (Gysi et al., 2011). The downloaded compositions were filtered to include only those samples for which Al_2O_3+CaO + K_2O + MgO + MnO + Na_2O + SiO_2+TiO_2+FeO^T summed to 98.5–101.5 wt. %. If a composition lacked an oxide measurement, that value was assumed to be zero. Figure 7 shows single-oxide histograms for the entire database. Before performing the thermodynamic calculations, the compositional data
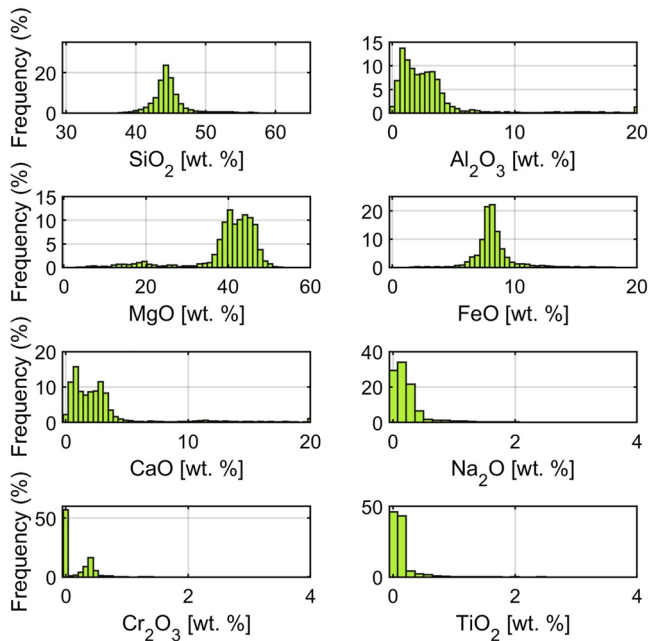
Figure 7. Compositional histograms for all 4,485 samples in the WISTFUL ultramafic database. Each histogram has 50 bins.

were renormalized to 100 wt. % in the NCFMASOCr system for the HGP solution models. We found that utilizing TiO_2 or K_2O data when available in thermodynamic calculations for the HGP model greatly increased the phase RMSE (~3 vol. %) and wave speed RMSE (~0.05 km/s) in comparison calculations. We present all thermodynamic calculations with two endmember equilibration temperatures (0°C and 800°C) for the choice of the reader, though the calculated seismic wave speeds are similar at low temperatures for both databases. Seismic wave speeds for each composition were calculated from 200 to 1,600°C and 0.5–7 GPa using a 157×157 grid. At *P-T* grid cells where calculations failed, values are linearly interpolated from surrounding cells.

4.2. Database Files

1. *WISTFUL_compositions_clean.mat*

This file contains the oxide composition (wt. %) for each rock in the database along with calculated Mg # and sample location data when available.

2. *WISTFUL_densities_clean.mat*

This file contains the calculated densities (kg m^{-3}) for all samples over the investigated range of pressure and temperature.

3. *WISTFUL_parsed_modes_clean.mat*

This file contains the calculated modal assemblage (olivine, orthopyroxene, clinopyroxene, garnet, spinel, other) (vol. %) for all samples over the investigated range of pressure and temperature.

4. *WISTFUL_rockType.mat*

This contains the rock-type defined by the renormalized olivine-orthopyroxene-clinopyroxene ternary using the calculated modes at 800°C and 2 GPa (Figure 8), resulting in 4,169 peridotite compositions and 457 pyroxenite compositions. Each rock type is stored as an integer corresponding to a rock type. The translation between integer and rock type is included in the readme.md file.

5. *WISTFUL_speeds_moduli_clean.mat*

This contains the anharmonic shear and bulk modulus (Pa), as well as V_p and V_s (km/s) for each rock in the database over the pressure (Pa) and temperature (K) range.

4.3. Anelastic Corrections

Olivine behaves anelastically at high temperature (>800°C) (Faul & Jackson, 2005a, 2015b; Jackson & Faul, 2010). Here, we assume that anelasticity only affects the shear modulus and that anelasticity calibrated on olivine samples can be applied to all ultramafic rocks based on recent experiments (Qu et al., 2021). For our databases, we allow users to choose between the extended-Burgers model fit of Jackson and Faul (2010), which combines a Maxwell element and a background element, and is dependent on pressure, temperature, period, and grain size; and the power-law fit of Behn et al. (2009), which is dependent on pressure, temperature, period, grain size, and water content. The Burgers model fit has been found to best fit laboratory data and attenuation estimates from geodetic and seismic measurements (Lau & Faul, 2019).

The Jackson and Faul (2010) anelasticity model excludes the effects of water, supported by recent experiments (Cline et al., 2018), but in contrast to previous experiments (Aizawa et al., 2008). Comparisons of measured and predicted quality factors prefer the inclusion of a water dependence to predict the G discontinuity (Behn et al., 2009; Karato & Park, 2018; Ma et al., 2020; Mark et al., 2021). Thus, we also enable the user to choose the power-law formulation of Behn et al. (2009), which includes a water dependence. We note the power-law anelasticity fails to fit experimental observations at low quality factors ($Q^{-1} > 0.1$) (Jackson & Faul, 2010). Further
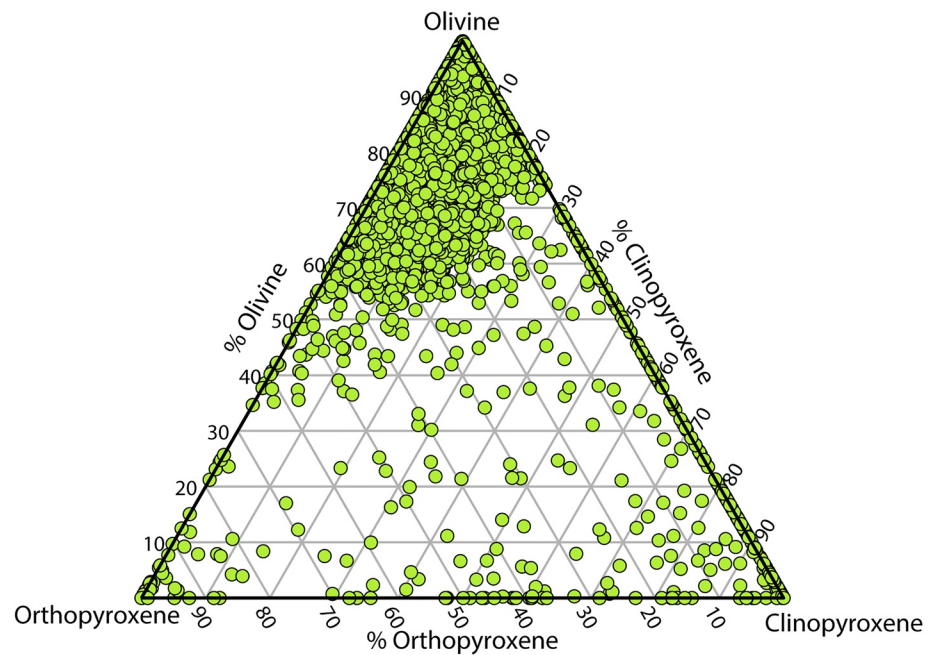
Figure 8. The WISTFUL ultramafic database plotted in the renormalized in the olivine-orthopyroxene-clinopyroxene ternary. Modes calculated with Perple_X at 800°C and 2 GPa using the Holland et al. (2018) solution models.

experiments are necessary to fully quantify the effects of water on anelasticity. Observed variations in anelasticity (Cline et al., 2018) with oxidation are also not considered here due to the minor variation in oxidation state present in the variable oxygen fugacity database. Anharmonic seismic wave speeds for all database compositions are available along with the following MATLAB® functions and live script to calculate anelastic corrections:

1. *behn2009shear.m, creep10.m, J1anel.m, J1p.m, J2anel.m, J2p.m*

These functions calculate the anelastic effects on the shear moduli described above. The latter five functions are shared courtesy of Ulrich Faul (pers. comm., 2021).

2. *calculateWaveSpeedFiles.mlx*

This live script loads in the uncorrected moduli in order to apply the user's choice of anelastic correction. To open and edit the live script, type and enter "edit *calculateWaveSpeedFiles.mlx*" in the MATLAB® command prompt while in the WISTFUL folder. The user chooses the anelasticity type using the drop-down menu. In addition, the user chooses the frequency, grain size, and water content for anelastic corrections by using the sliders or editing the numerical value left of the sliders by double clicking. The user can type the desired filename for the script to save the new data file. Saving the live script after editing will save these input changes. To create a corrected wave speed file, hit the "Run" button below the input section, after which the live script saves the corrected database as a new .mat file (Figure 9).

4.4. MATLAB® Function Files

1. *findClosestX.m*

This function inverts for temperature from input seismic wave speeds by finding the temperature at which the seismic misfit of the closest X samples is minimized, where the number X can be specified by the user. The misfit, Y, between the chosen seismic wave speed (one or two of V_S, V_p, and (V_p/V_s)) and the wave speed(s) predicted for each composition in the WISTFUL database $(V_{S_{WISTFUL}}, V_{P_{WISTFUL}}, (V_p/V_s)_{WISTFUL})$ is determined over all temperatures at a user specified input pressure. For example, if V_S and (V_p/V_s) are given, then
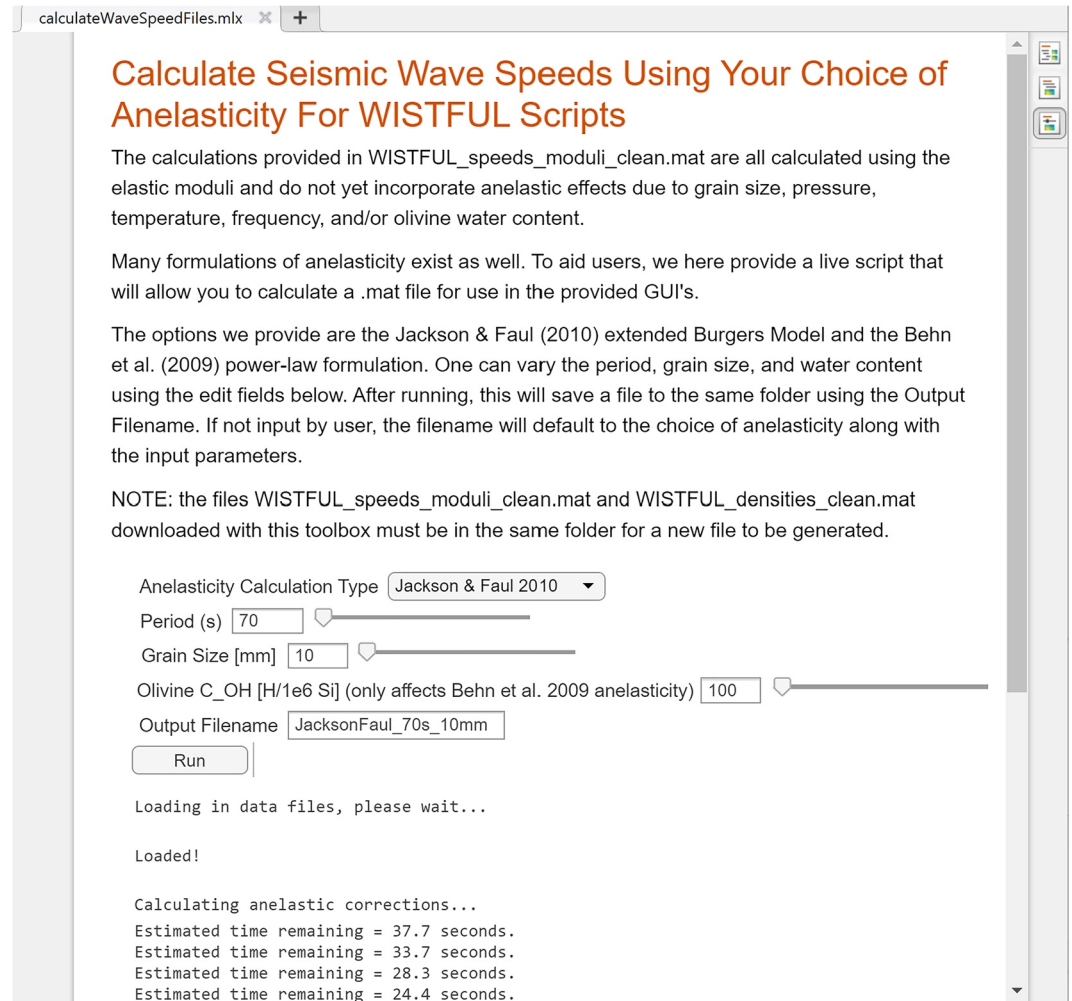
Figure 9. Snapshot of *calculateWaveSpeedFiles.mlx*. To reproduce this figure, open the live script by typing and entering "edit *calculateWaveSpeedFiles.mlx*" in MATLAB® command prompt while in the folder containing WISTFUL. To make the live script look the same, choose the "hide code option" button on the upper right of the MATLAB® editor, the bottom of the three button options. Then choose the dropdowns and enter the input parameters as written above, finally hitting the "Run" button to calculate and save the corrected wave speed file.

$$Y = \sqrt{\left(\frac{V_{\rm s} - V_{\rm s\,WISTFUL}}{V_{\rm s}}\right)^2 + \left(\frac{(V_{\rm p}/V_{\rm s}) - (V_{\rm p}/V_{\rm s})_{\rm WISTFUL}}{(V_{\rm p}/V_{\rm s})}\right)^2}. \tag{6}$$

At each temperature, an average misfit ($\overline{Y}_X$) is calculated as the mean of the X smallest misfits. The best-fit temperature ($T_{\rm B}$) is defined as the temperature with the minimum $\overline{Y}_X$. We define the uncertainty of $T_{\rm B}$ to be half of the range of all temperatures that fit the criteria

$$\overline{Y}_X^T < \overline{Y}_X^{T_{\rm B}} + \sigma_{Y_X^{T_{\rm B}}}, \tag{7}$$

where the superscript T denotes the temperature for $\overline{Y}_X$, and $\sigma_{Y_X^{T_{\rm B}}}$ is the standard deviation of the X smallest misfits at $T_{\rm B}$.

2. *fitPropertyClosestX.m*

This function returns the best-fit of a given compositional or physical property at the best-fit or other input temperature using the closest samples found from *findClosestX.m*. For instance, the best-fit density, ρ_B, Mg # (Mg#$_B$), or other compositional parameter, is calculated as the average of the that parameter from the X closest samples weighted by the reciprocal of the misfit of those samples at the best-fit temperature. For instance, Mg#$_B$ would be calculated as:

$$\text{Mg\#}_B = \frac{\sum_i \text{Mg\#}_i Y_i^{-1}}{\sum_i Y_i^{-1}}, \tag{8}$$

where subscript i denotes one of the closest X samples. We estimate the uncertainty for Mg#$_B$ as the average of the standard deviation of the Mg # weighted by $\overline{Y}_X^T$. These uncertainty estimates account for the distribution of wave speed misfit between the seismic and WISTFUL models, as well as the coarseness of the temperature values of the grid search.

3. *numWithinError.m*

This function inverts for temperature from input seismic wave speeds by determining how many samples within an input pressure and temperature range are within a specified wave speed misfit. Here we define misfit as the absolute percentage difference between the input wave speed and calculated sample wave speeds. This function calculates the number of WISTFUL samples within the specified misfit of seismic wave speed at each temperature within specified bounds. *numWithinError*.m then calculates the best-fit temperature as the mean of a Gaussian fit to the number of samples within the misfit. The function calculates the uncertainty as the standard deviation of the same Gaussian distribution.

4. *fitPropertyNumWithin.m*

This function returns a weighted average and standard deviation of an input property (e.g., Mg #) for all samples within a specified percentage misfit as described in *numWithinError.m* of a searched seismic wave speed at a given P and T. The mean and standard deviation is weighted by the inverse of the misfit as described above in *fitPropertyClosestX.m*.

4.5. MATLAB® Example Scripts

In addition to these functions, we provide two MATLAB® scripts to as examples of how to use the above functions from command line. The correct results are given as comments within the scripts to ensure the database files are loaded properly.

1. *exampleClosestX.m*

This script shows an example using *fitClosestX.m* and *fitPropertyClosestX.m*.

2. *exampleNumWithin.m*

This script shows an example use of the *numWithinError.m* and *fitPropertyNumWithin.m*.

5. General User Interfaces

WISTFUL contains three GUIs to investigate the compositional database designed with the MATLAB® App Designer.

1. *WISTFUL_relations.mlapp*

This GUI allows the user to investigate the distribution or relationship of two parameters at a given pressure and temperature (Figure 10). By default, the GUI loads the elastic seismic moduli from *WISTFUL_speeds_moduli_clean.mat*. If a user wishes to apply an anelastic correction, they must create a corrected wave speed file (see *calculateWaveSpeedFiles.mlx*) and load it into the GUI using the "Load Speed File" button in the top left corner. Once loaded, the text under the "Load Speed File" button will display the name of the loaded file.
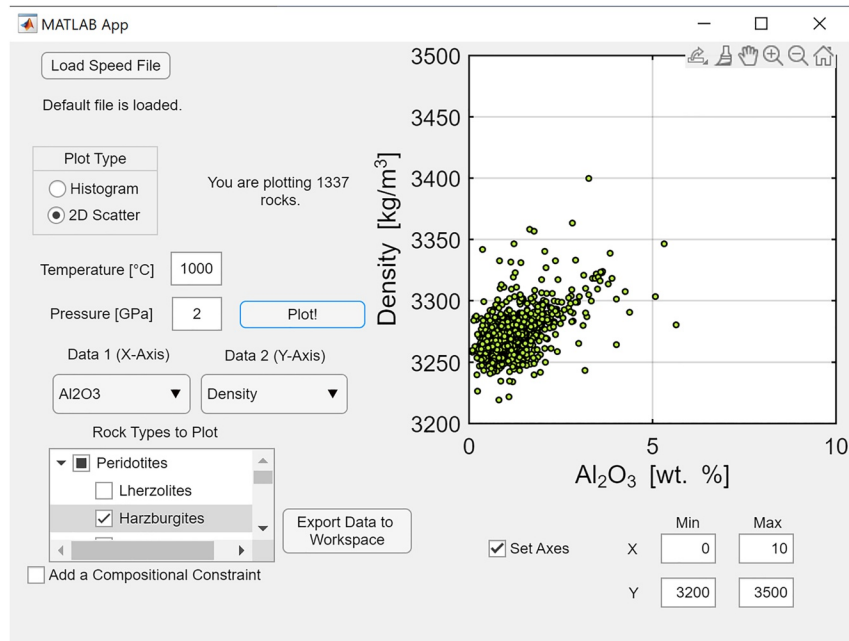
Figure 10. Snapshot of *WISTFUL_relations.mlapp* general user interfaces plotting a scatter plot of density against Al$_2$O$_3$ at 1,000°C and 2 GPa for the harzburgites in the database. To reproduce this figure, load *WISTFUL_relations.mlapp*. Choose the axes data, temperature, and pressure as shown. Limit the rock types plotted to only harzburgites. Click the "Add a compositional constraint" button and then select the drop-down menu, minimum, and maximum below as shown. Hit the "Plot!" button. Afterward, check the "Set Axes" checkbox and input the axes limits as shown.

Two different plots can be made using this GUI: (a) a histogram to show the distribution of a given parameter at a chosen temperature and pressure, and (b) relationships between two parameters for a subset of samples in the data. The plotted parameters are chosen in the drop-down menus on the left side. Plotted samples can be restricted by rock type or by a single compositional constraint using the rock type and additional constraints check boxes. The figure updates when you hit the "Plot!" button, at which point the text to the left of the figure will state how many samples are plotted. One can change the axes limits using the change axes interface in the bottom right. The "Export Data to Workspace" button allows for further investigation of the plotted datasets outside of the GUI. The steps required to reproduce the image seen in Figure 10 are detailed in caption.

2. *WISTFUL_geotherm.mlapp*

GUI that allows the user to investigate the seismic property of any given subset of rocks along a range of geotherms (Figure 11). By default, this GUI loads the elastic seismic moduli. To apply an anelastic correction, the user must create a corrected wavespeed file using *calculateWaveSpeedFiles.mlx* as described above and use the "Load Speed File" button in the top left corner. Standard geotherms such as a half-space cooling geotherm, a plate model geotherm, a continental geotherm with a constant heat production value are pre-coded into the GUI with the flexibility for users to specify parameters including ocean age, surface heat flux, or crustal heat productivity. Further input is allowed through the loading of a user-generated geotherm. For this functionality, the user must load a .mat file with vector files for depth (km), pressure (Pa), and temperature (°C) named as *z*, *p*, and *t* (case-sensitive). The loaded geotherm will be saved in the GUI until closed or another geotherm is loaded. The user can choose what rock types to plot, what property to plot, and what uncertainty to plot (mean only, range, mean with one or two standard deviations) using the drop-down menus on the left. The user can further select which rocks to plot by adding a single compositional constraint if desired. The "Plot!" button plots the input request. The axes can be changed by the max depth plotted, as well as the "Set Axes" functionality in the bottom right. The "Export Data to Workspace" button allows for further investigation of the plotted data outside of the GUI. The steps required to reproduce the image seen in Figure 11 are detailed in the caption.
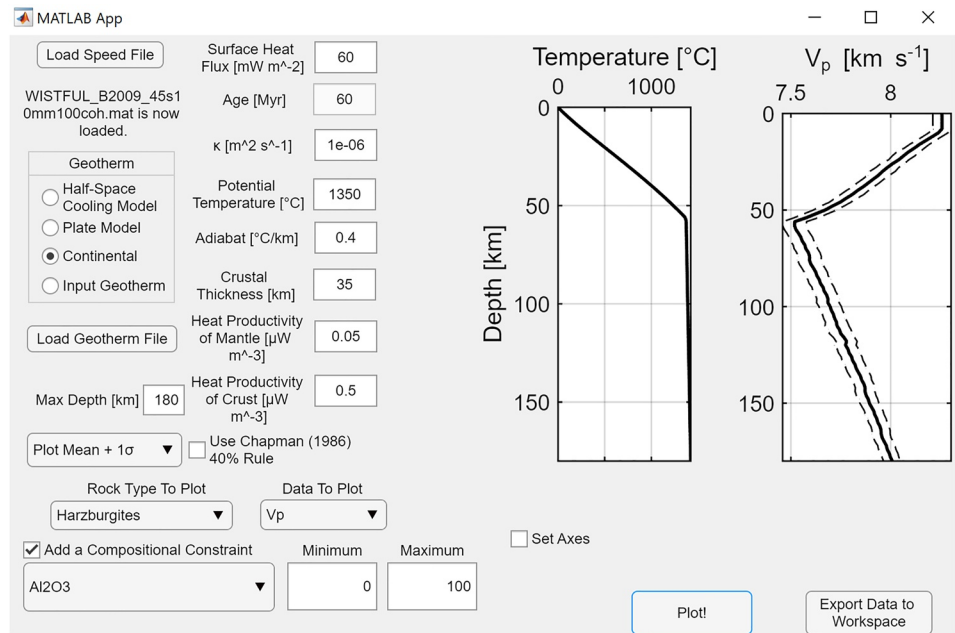
Figure 11. Snapshot of *WISTFUL_geotherm.mlapp* general user interfaces. To reproduce this figure, first create a wave speed file using *calculateWaveSpeedFiles.mlx* corrected for 10 mm grainsize, 100 ppm C_{OH}, and 45 s period using the Behn et al. (2009) anelasticity. Afterward open *WISTFUL_geotherm.mlapp*. Using the "Load Speed File" button, load in the corrected speed file described above. Then, set the text boxes and drop-down menus as shown. Finally, hit the "Plot!" button.

3. *WISTFUL_inversion.mlapp*

This GUI allows the user to invert for best-fit temperature and property using either of the fitting functions described above (Figure 12). Similar to the other GUIs, the user can load their choice of anelastic corrections and choose the rock type or compositional constraints for this inversion. For the inversion, the user can choose to fit to
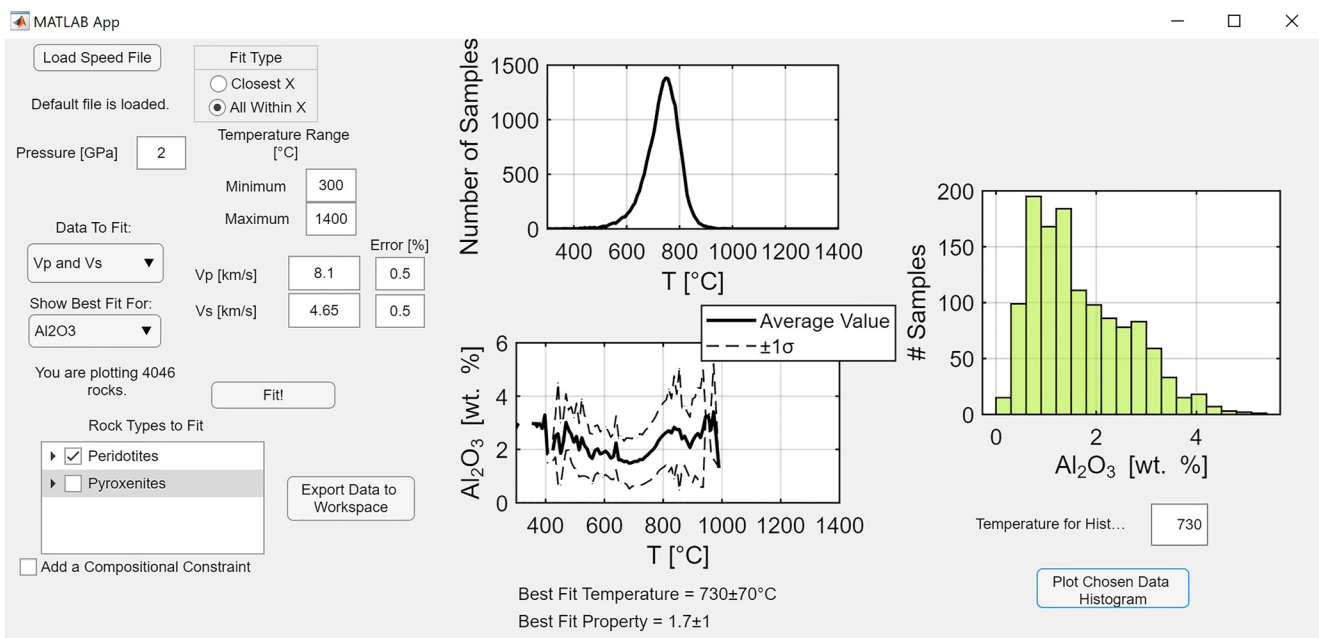

Figure 12. Snapshot of inversion general user interfaces. To reproduce this figure, first open *WISTFUL_inversion.mlapp*. Set the text and check boxes to be as seen to the left of the figures, with all types of peridotites checked. Then, set the text boxes and drop-downs as shown. Afterward, hit the Plot! button to plot the middle figures. Once plotted the Temperature for Histogram box will be automatically updated to the best-fit temperature. Finally, press the "Plot Chosen Data Histogram" button to plot the right-most figure.

V_p, V_s, V_p/V_s, or some combination. The user can also choose the temperature range as well as the extra property to fit. Once the options are chosen, the "Fit!" button plots the average RMSE using the closest X number of samples within error in the top middle figure. The lower figure depicts the best fit composition for each temperature. A text box on the left-hand side states how many samples are being used in the inversion due to the constraints given. The best-fit temperature and property value along with uncertainty are displayed beneath the middle figures. Further, the user can plot the histogram of the data at any single temperature using the "Plot Histogram!" button under the rightmost figure for any chosen temperature. After hitting the "Fit!" button, the "Temperature for Histogram" edit box will default to the best-fit temperature from the inversion. The "Export Data to Workspace" button allows for further investigation of the plotted data outside of the GUI. The steps required to reproduce the image seen in Figure 12 are detailed in caption.

Data Availability Statement

The toolbox is provided via a supplement and is available online (github.com/wshinevar/WISTFUL, https://doi.org/10.5281/zenodo.5815695).

References

Abers, G. A., & Hacker, B. R. (2016). A MATLAB toolbox and Excel workbook for calculating the densities, seismic wave speeds, and major element composition of minerals and rocks at pressure and temperature. *Geochemistry, Geophysics, Geosystems*, *17*(2), 616–624. https://doi.org/10.1002/2015GC006171

Afonso, J. C., Fernàndez, M., Ranalli, G., Griffin, W. L., & Connolly, J. A. D. (2008). Integrated geophysical-petrological modeling of the lithosphere and sublithospheric upper mantle: Methodology and applications. *Geochemistry, Geophysics, Geosystems*, *9*(5). https://doi.org/10.1029/2007GC001834

Afonso, J. C., Fullea, J., Griffin, W. L., Yang, Y., Jones, A. G., Connolly, J. A. D., & Reilly, S. Y. O. (2013). 3-D multiobservable probabilistic inversion for the compositional and thermal structure of the lithosphere and upper mantle. I: A priori petrological information and geophysical observables. *Journal of Geophysical Research: Solid Earth*, *118*(5), 2586–2617. https://doi.org/10.1002/jgrb.50124

Afonso, J. C., Fullea, J., Yang, Y., Connolly, J. A. D., & Jones, A. G. (2013). 3-D multi-observable probabilistic inversion for the compositional and thermal structure of the lithosphere and upper mantle. II: General methodology and resolution analysis. *Journal of Geophysical Research: Solid Earth*, *118*(4), 1650–1676. https://doi.org/10.1002/jgrb.50123

Afonso, J. C., Ranalli, G., Fernàndez, M., Griffin, W. L., O'Reilly, S. Y., & Faul, U. (2010). On the V_p/V_s-Mg# correlation in mantle peridotites: Implications for the identification of thermal and compositional anomalies in the upper mantle. *Earth and Planetary Science Letters*, *289*(3–4), 606–618. https://doi.org/10.1016/j.epsl.2009.12.005

Afonso, J. C., Rawlinson, N., Yang, Y., Schutt, D. L., Jones, A. G., Fullea, J., & Griffin, W. L. (2016). 3-D multiobservable probabilistic inversion for the compositional and thermal structure of the lithosphere and upper mantle: III. Thermochemical tomography in the western-Central U.S. *Journal of Geophysical Research: Solid Earth*, *121*(10), 7337–7370. https://doi.org/10.1002/2016JB013049

Aizawa, Y., Barnhoorn, A., Faul, U. H., Fitz Gerald, J. D., Jackson, I., & Kovács, I. (2008). Seismic properties of Anita Bay dunite: An exploratory study of the influence of water. *Journal of Petrology*, *49*(4), 841–855. https://doi.org/10.1093/petrology/egn007

Auer, L., Boschi, L., Becker, T. W., & Giardini, D. (2014). Savani: A variable resolution whole-mantle model of anisotropic shear velocity variations based, 3006–3034. https://doi.org/10.1002/2013JB010773

Babuška, V. (1972). Elasticity and anisotropy of dunite and bronzitite. *Journal of Geophysical Research*, *77*(35), 6955–6965. https://doi.org/10.1029/jb077i035p06955

Baptiste, V., Tommasi, A., & Demouchy, S. (2012). Deformation and hydration of the lithospheric mantle beneath the Kaapvaal craton, South Africa. *Lithos*, *149*, 31–50. https://doi.org/10.1016/j.lithos.2012.05.001

Bass, J. D. (1989). Elasticity of grossular and spessartite garnets by Brillouin spectroscopy. *Journal of Geophysical Research*, *94*(B6), 7621–7628. https://doi.org/10.1029/JB094iB06p07621

Behn, M. D., Hirth, G., & Elsenbeck, J. R. (2009). Implications of grain size evolution on the seismic structure of the oceanic upper mantle. *Earth and Planetary Science Letters*, *282*(1–4), 178–189. https://doi.org/10.1016/j.epsl.2009.03.014

Behn, M. D., & Kelemen, P. B. (2003). Relationship between seismic *P*-wave velocity and the composition of anhydrous igneous and meta-igneous rocks. *Geochemistry, Geophysics, Geosystems*, *4*(5), 1–57. https://doi.org/10.1029/2002GC000393

Behn, M. D., & Kelemen, P. B. (2006). Stability of arc lower crust: Insights from the Talkeetna arc section, south central Alaska, and the seismic structure of modern arcs. *Journal of Geophysical Research*, *111*(11), 1–20. https://doi.org/10.1029/2006JB004327

Bina, C. R., & Helffrich, G. R. (1992). Calculation of elastic properties from thermodynamic equation of state principles. *Annual Review of Earth and Planetary Sciences*, *20*(1), 527–552. https://doi.org/10.1146/annurev.earth.20.1.527

Birch, F. (1960). The velocity of compressional waves in rocks to 10 kilobars: 1. *Journal of Geophysical Research*, *65*(4), 1083–1102. https://doi.org/10.1029/JZ065i004p01083

Birch, F. (1961). The velocity of compressional waves in rocks to 10 kilobars: 2. *Journal of Geophysical Research*, *66*(7), 2199–2224. https://doi.org/10.1029/JZ066i007p02199

Borghini, G., Fumagalli, P., & Rampone, E. (2010). The stability of plagioclase in the upper mantle: Subsolidus experiments on fertile and depleted lherzolite. *Journal of Petrology*, *51*(1–2), 229–254. https://doi.org/10.1093/petrology/egp079

Brey, G. P., & Köhler, T. (1990). Geothermobarometry in four-phase lherzolites II. New thermobarometers, and practical assessment of existing thermobarometers. *Journal of Petrology*, *31*(6), 1353–1378. https://doi.org/10.1093/petrology/31.6.1353

Cammarano, F., Goes, S., Vacher, P., & Giardini, D. (2003). Inferring upper-mantle temperatures from seismic velocities. *Physics of the Earth and Planetary Interiors*, *138*(3–4), 197–222. https://doi.org/10.1016/S0031-9201(03)00156-0

Canil, D., O'Neill, H. S. C., Pearson, D. G., Rudnick, R. L., McDonough, W. F., & Carswell, D. A. (1994). Ferric iron in peridotites and mantle oxidation states. *Earth and Planetary Science Letters*, *123*(1–3), 205–220. https://doi.org/10.1016/0012-821X(94)90268-2

Christensen, N. I. (1966). Elasticity of ultrabasic rocks. *Journal of Geophysical Research*, *71*(24), 5921–5931. https://doi.org/10.1029/JZ071i024p05921

Christensen, N. I. (1974). Compressional wave velocities in possible the important relationship between density of which. *Journal of Geophysical Research*, *79*(2), 407–412. https://doi.org/10.1029/jb079i002p00407

Christensen, N. I. (1978). Ophiolites, seismic velocities and oceanic crustal structure. *Tectonophysics*, *47*(1–2), 131–157. https://doi.org/10.1016/0040-1951(78)90155-5

Christensen, N. I. (1979). Compressional wave velocities in rocks at high temperatures and pressures, critical thermal gradients, and crustal low-velocity zones. *Journal of Geophysical Research*, *84*(B12), 6849–6858. https://doi.org/10.1029/jb084ib12p06849

Christensen, N. I., & Ramananantoandro, R. (1971). Elastic moduli and anisotropy of dunite to 10 kilobars. *Journal of Geophysical Research*, *76*(17), 4003–4010. https://doi.org/10.1029/jb076i017p04003

Cline, C. J., Faul, U. H., David, E. C., Berry, A. J., & Jackson, I. (2018). Redox-influenced seismic properties of uppermantle olivine. *Nature*, *555*(7696), 355–358. https://doi.org/10.1038/nature25764

Connolly, J. A. D. (2009). The geodynamic equation of state: What and how. *Geochemistry, Geophysics, Geosystems*, *10*(10). https://doi.org/10.1029/2009GC002540

Connolly, J. A. D., & Khan, A. (2016). Uncertainty of mantle geophysical properties computed from phase equilibrium models. *Geophysical Research Letters*, *43*(10), 5026–5034. https://doi.org/10.1002/2016GL068239

Cottrell, E., & Kelley, K. A. (2011). The oxidation state of Fe in MORB glasses and the oxygen fugacity of the upper mantle. *Earth and Planetary Science Letters*, *305*(3–4), 270–282. https://doi.org/10.1016/j.epsl.2011.03.014

De Capitani, C., & Petrakakis, K. (2010). The computation of equilibrium assemblage diagrams with Theriak/Domino software. *American Mineralogist*, *95*(7), 1006–1016. https://doi.org/10.2138/am.2010.3354

Demouchy, S., Ishikawa, A., Tommasi, A., Alard, O., & Keshav, S. (2015). Characterization of hydration in the mantle lithosphere: Peridotite xenoliths from the Ontong Java Plateau as an example. *Lithos*, *212*, 189–201. https://doi.org/10.1016/j.lithos.2014.11.005

Diaferia, G., & Cammarano, F. (2017). Seismic signature of the continental crust: What thermodynamics says. An example from the Italian Peninsula. *Tectonics*, *36*(12), 3192–3208. https://doi.org/10.1002/2016TC004405

Diaferia, G., Cammarano, F., Piana Agostinetti, N., Gao, C., Lekic, V., Molinari, I., & Boschi, L. (2019). Inferring crustal temperatures beneath Italy from joint inversion of receiver functions and surface waves. *Journal of Geophysical Research: Solid Earth*, *124*(8), 8771–8785. https://doi.org/10.1029/2019JB018340

Duffy, T. S., & Anderson, D. L. (1989). Seismic velocities in mantle minerals and the mineralogy of the upper mantle. *Journal of Geophysical Research*, *94*(B2), 1895–1912. https://doi.org/10.1029/JB094iB02p01895

Falus, G., Tommasi, A., Ingrin, J., & Szabó, C. (2008). Deformation and seismic anisotropy of the lithospheric mantle in the southeastern Carpathians inferred from the study of mantle xenoliths. *Earth and Planetary Science Letters*, *272*(1–2), 50–64. https://doi.org/10.1016/j.epsl.2008.04.035

Fan, D., Fu, S., Yang, J., Tkachev, S. N., Prakapenka, V. B., & Lin, J. F. (2019). Elasticity of single-crystal periclase at high pressure and temperature: The effect of iron on the elasticity and seismic parameters of ferropericlase in the lower mantle. *American Mineralogist*, *104*(2), 262–275. https://doi.org/10.2138/am-2019-6656

Faul, U., & Jackson, I. (2005a). The seismological signature of temperature and grain size variations in the upper mantle. *Earth and Planetary Science Letters*, *234*(1–2), 119–134. https://doi.org/10.1016/j.epsl.2005.02.008

Faul, U., & Jackson, I. (2015b). Transient creep and strain energy dissipation: An experimental perspective. *Annual Review of Earth and Planetary Sciences*, *43*(1), 541–569. https://doi.org/10.1146/annurev-earth-060313-054732

Fountain, D. M., & Christensen, N. I. (1989). Chapter 30: Composition of the continental crust and upper mantle: A review. In *Memoir of the Geological Society of America* (Vol. 172, pp. 711–742). https://doi.org/10.1130/MEM172-p711

Fullea, J., Afonso, J. C., Connolly, J. A. D., Fernàndez, M., García-Castellanos, D., & Zeyen, H. (2009). LitMod3D: An interactive 3-D software to model the thermal, compositional, density, seismological, and rheological structure of the lithosphere and sublithospheric upper mantle. *Geochemistry, Geophysics, Geosystems*, *10*(8), 1–21. https://doi.org/10.1029/2009GC002391

Fullea, J., Lebedev, S., Martinec, Z., & Celli, N. L. (2021). WINTERC-G: Mapping the upper mantle thermochemical heterogeneity from coupled geophysical–petrological inversion of seismic waveforms, heat flow, surface elevation and gravity satellite data. *Geophysical Journal International*, *226*(1), 146–191. https://doi.org/10.1093/gji/ggab094

Gao, S., Kern, H., Liu, Y. S., Jin, S. Y., Popp, T., Jin, Z. M., et al. (2000). Measured and calculated seismic velocities and densities for granulites from xenolith occurrences and adjacent exposed lower crustal sections: A comparative study from the North China craton. *Journal of Geophysical Research*, *105*(B8), 18965–18976. https://doi.org/10.1029/2000jb900100

Goes, S., Govers, R., & Vacher, P. (2000). Shallow mantle temperatures under Europe from P and S wave tomography. *Journal of Geophysical Research*, *105*(B5), 11153–11169. https://doi.org/10.1029/1999jb900300

Goes, S., & van der Lee, S. (2002). Thermal structure of the North American uppermost mantle inferred from seismic tomography. *Journal of Geophysical Research*, *107*(B3), 2050. https://doi.org/10.1029/2000jb000049

Golos, E. M., Fang, H., & van der Hilst, R. D. (2020). Variations in seismic wave speed and V_P/V_S ratio in the North American lithosphere. *Journal of Geophysical Research: Solid Earth*, *125*(12), e2020JB020574. https://doi.org/10.1029/2020JB020574

Gréaux, S., & Yamada, A. (2019). Density variations of Cr-rich garnets in the upper mantle inferred from the elasticity of uvarovite garnet. *Comptes Rendus Geoscience*, *351*(2–3), 95–103. https://doi.org/10.1016/j.crte.2018.09.012

Green, D. H., & Ringwood, A. E. (1970). Mineralogy of peridotitic compositions under upper mantle conditions. *Physics of the Earth and Planetary Interiors*, *3*(C), 359–371. https://doi.org/10.1016/0031-9201(70)90076-2

Gysi, A. P., Jagoutz, O., Schmidt, M., & Targuisti, K. (2011). Petrogenesis of pyroxenites and melt infiltrations in the ultramafic complex of Beni Bousera, northern Morocco. *Journal of Petrology*, *52*(9), 1679–1735. https://doi.org/10.1093/petrology/egr026

Hacker, B. R., & Abers, G. A. (2004). Subduction Factory 3: An Excel worksheet and macro for calculating the densities, seismic wave speeds, and H_2O contents of minerals and rocks at pressure and temperature. *Geochemistry, Geophysics, Geosystems*, *5*(1), 1–7. https://doi.org/10.1029/2003GC000614

Hacker, B. R., Abers, G. A., & Peacock, S. M. (2003). Subduction factory 1. Theoretical mineralogy, densities, seismic wave speeds, and H_2O contents. *Journal of Geophysical Research*, *108*(B1), 1–26. https://doi.org/10.1029/2001jb001127

Hacker, B. R., Peacock, S. M., Abers, G. A., & Holloway, S. D. (2003). Subduction factory 2. Are intermediate-depth earthquakes in subducting slabs linked to metamorphic dehydration reactions? *Journal of Geophysical Research*, *108*(B1), 2030. https://doi.org/10.1029/2001jb001129

Hammond, W. C., & Humphreys, E. D. (2000). Upper mantle seismic wave attenuation: Effects of realistic partial melt distribution. *Journal of Geophysical Research*, *105*(B5), 10987–10999. https://doi.org/10.1029/2000jb900042

Helffrich, G. R., Stein, S., & Wood, B. J. (1989). Subduction zone thermal structure and mineralogy and their relationship to seismic wave reflections and conversions at the slab/mantle interface. *Journal of Geophysical Research*, *94*(B1), 753. https://doi.org/10.1029/JB094iB01p00753

Hill, R. (1952). The elastic behaviour of a crystalline aggregate. *Proceedings of the Physical Society Section A*, *65*(5), 349–354. https://doi.org/10.1088/0370-1298/65/5/307

Holland, T., & Powell, R. (1996). Thermodynamics of order-disorder in minerals: II. Symmetric formalism applied to solid solutions. *American Mineralogist*, *81*(11–12), 1425–1437. https://doi.org/10.2138/am-1996-11-1215

Holland, T., & Powell, R. (2003). Activity-composition relations for phases in petrological calculations: An asymmetric multicomponent formulation. *Contributions to Mineralogy and Petrology*, *145*(4), 492–501. https://doi.org/10.1007/s00410-003-0464-z

Holland, T. J. B., Green, E. C. R., & Powell, R. (2018). Melting of peridotites through to granites: A simple thermodynamic model in the system KNCFMASHTOCr. *Journal of Petrology*, *59*(5), 881–900. https://doi.org/10.1093/petrology/egy048

Holland, T. J. B., & Powell, R. (1998). An internally consistent thermodynamic data set for phases of petrological interest. *Journal of Metamorphic Geology*, *16*(3), 309–343. https://doi.org/10.1111/j.1525-1314.1998.00140.x

Holland, T. J. B., & Powell, R. (2011). An improved and extended internally consistent thermodynamic dataset for phases of petrological interest, involving a new equation of state for solids. *Journal of Metamorphic Geology*, *29*(3), 333–383. https://doi.org/10.1111/j.1525-1314.2010.00923.x

Ionov, D. A., Doucet, L. S., & Ashchepkov, I. V. (2010). Composition of the lithospheric mantle in the siberian craton: New constraints from fresh peridotites in the Udachnaya-East Kimberlite. *Journal of Petrology*, *51*(11), 2177–2210. https://doi.org/10.1093/petrology/egq053

Jackson, I., & Faul, U. H. (2010). Grainsize-sensitive viscoelastic relaxation in olivine: Towards a robust laboratory-based model for seismological application. *Physics of the Earth and Planetary Interiors*, *183*(1–2), 151–163. https://doi.org/10.1016/j.pepi.2010.09.005

Jagoutz, O., & Behn, M. D. (2013). Foundering of lower island-arc crust as an explanation for the origin of the continental Moho. *Nature*, *504*(7478), 131–134. https://doi.org/10.1038/nature12758

Jennings, E. S., & Holland, T. J. B. (2015). A simple thermodynamic model for melting of peridotite in the system NCFMASOCr. *Journal of Petrology*, *56*(5), 869–892. https://doi.org/10.1093/petrology/egv020

Jiang, F., Speziale, S., Shieh, S. R., & Duffy, T. S. (2004). Single-crystal elasticity of andradite garnet to 11 GPa. *Journal of Physics: Condensed Matter*, *16*(14), S1041–S1052. https://doi.org/10.1088/0953-8984/16/14/014

Jones, A. G., Afonso, J. C., & Fullea, J. (2017). Geochemical and geophysical constrains on the dynamic topography of the Southern African Plateau. *Geochemistry, Geophysics, Geosystems*, *18*(10), 3556–3575. https://doi.org/10.1002/2017GC006908

Jordan, T. H. (1979). Mineralogies, densities and seismic velocities of garnet lherzolites and their geophysical implications. In *The mantle sample: Inclusion in Kimberlites and other Volcanics* (pp. 1–14). American Geophysical Union. https://doi.org/10.1029/SP016p0001

Kaban, M. K., Tesauro, M., Mooney, W. D., & Cloetingh, S. A. P. L. (2014). Density, temperature, and composition of the North American lithosphere—New insights from a joint analysis of seismic, gravity, and mineral physics data: 1. Density structure of the crust and upper mantle. *Geochemistry, Geophysics, Geosystems*, *15*(12), 4781–4807. https://doi.org/10.1002/2014GC005483

Karato, S. (1993). Importance of anelasticity in the interpretation of seismic tomography. *Geophysical Research Letters*, *20*(15), 1623–1626. https://doi.org/10.1029/93GL01767

Karato, S. I., & Park, J. (2018). On the origin of the upper mantle seismic discontinuities. *Lithospheric Discontinuities*, 5–34. https://doi.org/10.1002/9781119249740.ch1

Kelemen, P. B., & Holbrook, W. S. (1995). Origin of thick, high-velocity igneous crust along the US East Coast Margin. *Journal of Geophysical Research*, *100*(B6), 10077–10094. https://doi.org/10.1029/95jb00924

Kern, H., Gao, S., & Liu, Q.-S. (1996). Seismic properties and densities of middle and lower crustal rocks exposed along the North China Geoscience Transect. *Earth and Planetary Science Letters*, *139*(3–4), 439–455. https://doi.org/10.1016/0012-821X(95)00240-D

Khan, A. (2016). On Earth's mantle Constitution and structure from joint analysis of geophysical and laboratory-based data: An example. *Surveys in Geophysics*, *37*(1), 149–189. https://doi.org/10.1007/s10712-015-9353-z

Khan, A., Koch, S., Shankland, T. J., Zunino, A., & Connolly, J. A. D. (2015). Relationships between seismic wave-speed, density, and electrical conductivity beneath Australia from seismology, mineralogy, and laboratory-based conductivity profiles. In *The Earth's heterogeneous mantle* (pp. 145–171). Springer International Publishing. https://doi.org/10.1007/978-3-319-15627-9_5

Khan, A., Zunino, A., & Deschamps, F. (2011). The thermo-chemical and physical structure beneath the North American continent from Bayesian inversion of surface-wave phase velocities. *Journal of Geophysical Research*, *116*(9), 1–23. https://doi.org/10.1029/2011JB008380

Klemme, S. (2004). The influence of Cr on the garnet-spinel transition in the Earth's mantle: Experiments in the system $MgO-Cr_2O_3-SiO_2$ and thermodynamic modelling. *Lithos*, *77*(1–4), 639–646. https://doi.org/10.1016/j.lithos.2004.03.017

Klemme, S., Ivanic, T. J., Connolly, J. A. D., & Harte, B. (2009). Thermodynamic modelling of Cr-bearing garnets with implications for diamond inclusions and peridotite xenoliths. *Lithos*, *112*, 986–991. https://doi.org/10.1016/j.lithos.2009.05.007

Kono, Y., Ishikawa, M., & Arima, M. (2004). Discontinuous change in temperature derivative of V_p in lower crustal rocks. *Geophysical Research Letters*, *31*(22), 1–4. https://doi.org/10.1029/2004GL020964

Kono, Y., Ishikawa, M., Harigane, Y., Michibayashi, K., & Arima, M. (2009). P- and S-wave velocities of the lowermost crustal rocks from the Kohistan arc: Implications for seismic Moho discontinuity attributed to abundant garnet. *Tectonophysics*, *467*(1–4), 44–54. https://doi.org/10.1016/j.tecto.2008.12.010

Kretz, R. (1982). Transfer and exchange equilibria in a portion of the pyroxene quadrilateral as deduced from natural and experimental data. *Geochimica et Cosmochimica Acta*, *46*(3), 411–421. https://doi.org/10.1016/0016-7037(82)90232-0

Kroenke, L. W., Manghnani, M. H., Rai, C. S., Fryer, P., & Ramananantoandro, R. (1976). Elastic properties of selected ophiolitic rocks from Papua New Guinea: Nature and composition of oceanic lower crust and upper mantle. *The Geophysics of the Pacific Ocean Basin and Its Margin*, *19*, 407–421. https://doi.org/10.1029/GM019p0407

Kumar, A., Fernàndez, M., Jiménez-Munt, I., Torne, M., Vergés, J., & Afonso, J. C. (2020). LitMod2D_2.0: An improved integrated geophysical-petrological modeling tool for the physical interpretation of upper mantle anomalies. *Geochemistry, Geophysics, Geosystems*, *21*(3), 1–19. https://doi.org/10.1029/2019GC008777

Kuskov, O. L., Kronrod, V. A., & Annersten, H. (2006). Inferring upper-mantle temperatures from seismic and geochemical constraints: Implications for Kaapvaal craton. *Earth and Planetary Science Letters*, *244*(1–2), 133–154. https://doi.org/10.1016/j.epsl.2006.02.016

Kuskov, O. L., Kronrod, V. A., & Kronrod, E. V. (2014). Thermo-chemical constraints on the interior structure and composition of the lunar mantle. *Physics of the Earth and Planetary Interiors*, *235*, 84–95. https://doi.org/10.1016/j.pepi.2014.07.011

Kuskov, O. L., Kronrod, V. A., Prokofyev, A. A., & Pavlenkova, N. I. (2014). Thermo-chemical structure of the lithospheric mantle underneath the Siberian craton inferred from long-range seismic profiles. *Tectonophysics*, *615*, 154–166. https://doi.org/10.1016/j.tecto.2014.01.006

Lau, H. C. P., & Faul, U. H. (2019). Anelasticity from seismic to tidal timescales: Theory and observations. *Earth and Planetary Science Letters*, *508*, 18–29. https://doi.org/10.1016/j.epsl.2018.12.009

Lee, C.-T., & Rudnick, R. L. (1999). Compositionally stratified cratonic lithosphere: Petrology and geochemistry of peridotite xenoliths from the Labait tuff cone, Tanzania. In *International Kimberlite Conference, (February)* (pp. 503–521).

Lee, C.-T. A. (2003). Compositional variation of density and seismic velocities in natural peridotites at STP conditions: Implications for seismic imaging of compositional heterogeneities in the upper mantle. *Journal of Geophysical Research*, *108*(B9), 2441. https://doi.org/10.1029/2003jb002413

Liebermann, R. C., Jackson, I., & Ringwood, A. E. (1977). Elasticity and phase equilibria of spinel disproportionation reactions. *Geophysical Journal of the Royal Astronomical Society*, *50*(3), 553–586. https://doi.org/10.1111/j.1365-246X.1977.tb01335.x

Ma, Z., Dalton, C. A., Russell, J. B., Gaherty, J. B., Hirth, G., & Forsyth, D. W. (2020). Shear attenuation and anelastic mechanisms in the central Pacific upper mantle. *Earth and Planetary Science Letters*, *536*, 116148. https://doi.org/10.1016/j.epsl.2020.116148

Malaspina, N., Poli, S., & Fumagalli, P. (2009). The oxidation state of metasomatized mantle wedge: Insights from C-O-H-bearing garnet peridotite. *Journal of Petrology*, *50*(8), 1533–1552. https://doi.org/10.1093/petrology/egp040

Mao, N., Ito, J., Hays, J. F., Drake, J., & Birch, F. (1970). Composition and elastic constants of Hortonolite dunite. *Journal of Geophysical Research*, *75*(20), 4071–4076. https://doi.org/10.1029/JB075i020p04071

Mark, H. F., Collins, J. A., Lizarralde, D., Hirth, G., Gaherty, J. B., Evans, R. L., & Behn, M. D. (2021). Constraints on the depth, thickness, and strength of the G discontinuity in the central Pacific from S receiver functions. *Journal of Geophysical Research: Solid Earth*, *126*(4), e2020JB021219. https://doi.org/10.1029/2019JB019256

Matsukage, K. N., Kikuchi, S., Ono, S., Nishihara, Y., & Kikegawa, T. (2010). Density and seismic velocities of chromitite body in oceanic mantle peridotite. *American Mineralogist*, *95*(10), 1422–1428. https://doi.org/10.2138/am.2010.3498

Miller, D. J., & Christensen, N. I. (1994). Seismic signature and geochemistry of an island arc: A multidisciplinary study of the Kohistan accreted terrane, northern Pakistan. *Journal of Geophysical Research*, *99*(B6), 11623–11642. https://doi.org/10.1029/94jb00059

Mori, T., & Green, D. H. (1978). Laboratory duplication of phase equilibria observed in natural garnet lherzolites. *The Journal of Geology*, *86*(1), 83–97. https://doi.org/10.1086/649657

Nestola, F., Periotto, B., Andreozzi, G. B., Bruschini, E., & Bosi, F. (2014). Pressure-volume equation of state for chromite and magnesiochromite: A single-crystal X-ray diffraction investigation. *American Mineralogist*, *99*(7), 1248–1253. https://doi.org/10.2138/am.2014.4765

Nickel, K. G., & Green, D. H. (1985). Empirical geothermobarometry for garnet peridotites and implications for the nature of the lithosphere, kimberlites and diamonds. *Earth and Planetary Science Letters*, *73*(1), 158–170. https://doi.org/10.1016/0012-821X(85)90043-3

O'Reilly, S. Y., Jackson, I., & Bezant, C. (1990). Equilibration temperatures and elastic wave velocities for upper mantle rocks from eastern Australia: Implications for the interpretation of seismological models. *Tectonophysics*, *185*(1–2), 67–82. https://doi.org/10.1016/0040-1951(90)90405-W

Pavese, A., Diella, V., Pischedda, V., Merli, M., Bocchio, R., & Mezouar, M. (2001). Pressure-volume-temperature equation of state of andradite and grossular, by high-pressure and -temperature powder diffraction. *Physics and Chemistry of Minerals*, *28*(4), 242–248. https://doi.org/10.1007/s002690000144

Peercy, M. S., & Bass, J. D. (1990). Elasticity of monticellite. *Physics and Chemistry of Minerals*, *17*(5), 431–437. https://doi.org/10.1007/BF00212212

Perry, H. K. C., Forte, A. M., & Eaton, D. W. S. (2003). Upper-mantle thermochemical structure below North America from seismic-geodynamic flow models. *Geophysical Journal International*, *154*(2), 279–299. https://doi.org/10.1046/j.1365-246X.2003.01961.x

Peselnick, L., & Nicolas, A. (1978). Seismic anisotropy in an ophiolite peridotite: Application to oceanic upper mantle. *Journal of Geophysical Research*, *83*(B3), 1227. https://doi.org/10.1029/jb083ib03p01227

Posner, E. S., Dera, P., Downs, R. T., Lazarz, J. D., & Irmen, P. (2014). High-pressure single-crystal X-ray diffraction study of jadeite and kosmochlor. *Physics and Chemistry of Minerals*, *41*(9), 695–707. https://doi.org/10.1007/s00269-014-0684-y

Powell, R., & Holland, T. (1994). Optimal geothermometry and geobarometry Rocnn. *American Mineralogist*, *79*(1992), 120–133.

Powell, R., & Holland, T. (1999). Relating formulations of the thermodynamics of mineral solid solutions: Activity modeling of pyroxenes, amphiboles, and micas. *American Mineralogist*, *84*(1–2), 1–14. https://doi.org/10.2138/am-1999-1-201

Prelicz, R. M. (2005). *Seismic anisotropy in peridotites from the Western Gneiss Region (Norway): Laboratory measurements at high PT conditions and fabric based model predictions, Doctoral dissertation*. ETH Zurich. https://doi.org/10.3929/ethz-a-005115293

Priestley, K., & McKenzie, D. (2013). The relationship between shear wave velocity, temperature, attenuation and viscosity in the shallow part of the mantle. *Earth and Planetary Science Letters*, *381*, 78–91. https://doi.org/10.1016/j.epsl.2013.08.022

Qu, T., Jackson, I., & Faul, U. H. (2021). Low-frequency seismic properties of olivine-orthopyroxene mixtures. *Journal of Geophysical Research: Solid Earth*, *126*(10), e2021JB022504. https://doi.org/10.1029/2021JB022504

Ramana, Y. V., & Rao, M. V. M. S. (1974). Compressional velocities in ultramafic rocks of India at pressures to five kilobars. *Geophysical Journal of the Royal Astronomical Society*, *37*(1), 207–212. https://doi.org/10.1111/j.1365-246X.1974.tb02453.x

Reuss, A. (1928). Berechnung der Fliehgrenze von Mischkristallen auf Grund der Plastizittitsbedingung fiir Einkristalle. *ZAMM-Journal of Applied Mathematics and Mechanics*, *9*, 49–58.

Ritsema, J., Deuss, A., Van Heijst, H. J., & Woodhouse, J. H. (2011). S40RTS: A degree-40 shear-velocity model for the mantle from new Rayleigh wave dispersion, teleseismic traveltime and normal-mode splitting function measurements. *Geophysical Journal International*, *184*(3), 1223–1236. https://doi.org/10.1111/j.1365-246X.2010.04884.x

Rudnick, R. L., & Fountain, D. M. (1995). Nature and composition of the continental crust: A lower crustal perspective. *Reviews of Geophysics*, *33*(3), 267–309. https://doi.org/10.1029/95RG01302

Sammon, L. G., Gao, C., & McDonough, W. F. (2020). Lower crustal composition in the southwestern United States. *Journal of Geophysical Research: Solid Earth*, *125*(3), 1–14. https://doi.org/10.1029/2019JB019011

Schutt, D. L., & Lesher, C. E. (2006). Effects of melt depletion on the density and seismic velocity of garnet and spinel lherzolite. *Journal of Geophysical Research*, *111*(5), 1–24. https://doi.org/10.1029/2003JB002950

Schutt, D. L., & Lesher, C. E. (2010). Compositional trends among Kaapvaal Craton garnet peridotite xenoliths and their effects on seismic velocity and density. *Earth and Planetary Science Letters*, *300*(3–4), 367–373. https://doi.org/10.1016/j.epsl.2010.10.018

Schutt, D. L., Lowry, A. R., & Buehler, J. S. (2018). Moho temperature and mobility of lower crust in the western United States. *Geology*, *46*(3), 219–222. https://doi.org/10.1130/G39507.1

Shan, B., Zhou, W., & Xiao, Y. (2021). Lithospheric thermal and compositional structure of South China jointly inverted from multiple geophysical observations. *Science China Earth Sciences*, *64*(1), 148–160. https://doi.org/10.1007/s11430-019-9661-4

Sharp, Z. D., Hazen, R. M., & Finger, L. W. (1987). High-pressure crystal chemistry of monticellite, $CaMgSiO_4$. *American Mineralogist*, *72*, 748–755.

Shen, W., & Ritzwoller, M. H. (2016). Crustal and uppermost mantle structure beneath the United States. *Journal of Geophysical Research: Solid Earth*, *121*(6), 4306–4342. https://doi.org/10.1002/2016JB012887

Simmons, N. A., Forte, A. M., Boschi, L., & Grand, S. P. (2010). GyPSuM: A joint tomographic model of mantle density and seismic wave speeds. *Journal of Geophysical Research*, *115*(12), 1–24. https://doi.org/10.1029/2010JB007631

Simmons, N. A., Forte, A. M., & Grand, S. P. (2009). Joint seismic, geodynamic and mineral physical constraints on three-dimensional mantle heterogeneity: Implications for the relative importance of thermal versus compositional heterogeneity. *Geophysical Journal International*, *177*(3), 1284–1304. https://doi.org/10.1111/j.1365-246X.2009.04133.x

Sobolev, S. V., & Babeyko, A. Y. (1989). Phase transformations in the lower continental crust and its seismic structure. *Properties and Processes of Earth' Lower Crust*, *51*, 311–320. https://doi.org/10.1029/gm051p0311

Sobolev, S. V., & Babeyko, A. Y. U. (1994). Modeling of mineralogical composition, density and elastic wave velocities in anhydrous magmatic rocks. *Surveys in Geophysics*, *15*(1961), 515–544. https://doi.org/10.1007/bf00690173

Sobolev, S. V., Zeyen, H., Granet, M., Achauer, U., Bauer, C., Werling, F., et al. (1997). Upper mantle temperatures and lithosphere-asthenosphere system beneath the French Massif Central constrained by seismic, gravity, petrologic and thermal observations. *Tectonophysics*, *275*(1–3), 143–164. https://doi.org/10.1016/S0040-1951(97)00019-X

Sobolev, S. V., Zeyen, H., Stoll, G., Werling, F., Altherr, R., & Fuchs, K. (1996). Upper mantle temperatures from teleseismic tomography of French Massif Central including effects of composition, mineral reactions, anharmonicity, anelasticity and partial melt. *Earth and Planetary Science Letters*, *139*(1–2), 147–163. https://doi.org/10.1016/0012-821x(95)00238-8

Stixrude, L., & Lithgow-Bertelloni, C. (2005). Thermodynamics of mantle minerals—I. Physical properties. *Geophysical Journal International*, *162*(2), 610–632. https://doi.org/10.1111/j.1365-246X.2005.02642.x

Stixrude, L., & Lithgow-Bertelloni, C. (2011). Thermodynamics of mantle minerals—II. Phase equilibria. *Geophysical Journal International*, *184*(3), 1180–1213. https://doi.org/10.1111/j.1365-246X.2010.04890.x

Syono, Y., Fukai, Y., & Ishikawa, Y. (1971). Anomalous elastic properties of Fe_2TiO_4. *Journal of the Physical Society of Japan*, *31*(2), 471–476. https://doi.org/10.1143/JPSJ.31.471

Tesauro, M., Kaban, M. K., Mooney, W. D., & Cloetingh, S. A. P. L. (2014). Density, temperature, and composition of the North American lithosphere-New insights from a joint analysis of seismic, gravity, and mineral physics data: 2. Thermal and compositional model of the upper mantle. *Geochemistry, Geophysics, Geosystems*, *15*(12), 4808–4830. https://doi.org/10.1002/2014gc005484

Tommasi, A., Godard, M., Coromina, G., Dautria, J. M., & Barsczus, H. (2004). Seismic anisotropy and compositionally induced velocity anomalies in the lithosphere above mantle plumes: A petrological and microstructural study of mantle xenoliths from French Polynesia. *Earth and Planetary Science Letters*, *227*(3–4), 539–556. https://doi.org/10.1016/j.epsl.2004.09.019

Tommasi, A., & Ishikawa, A. (2014). Microstructures, composition, and seismic properties of the Ontong Java Plateau mantle root. *Geochemistry, Geophysics, Geosystems*, *15*(11), 4547–4569. https://doi.org/10.1002/2014GC005452

Tommasi, A., Vauchez, A., & Ionov, D. A. (2008). Deformation, static recrystallization, and reactive melt transport in shallow subcontinental mantle xenoliths (Tok Cenozoic volcanic field, SE Siberia). *Earth and Planetary Science Letters*, *272*(1–2), 65–77. https://doi.org/10.1016/j.epsl.2008.04.020

Tunini, L., Jiménez-Munt, I., Fernandez, M., Vergés, J., & Villaseñor, A. (2014). Lithospheric mantle heterogeneities beneath the Zagros mountains and the Iranian plateau: A petrological-geophysical study. *Geophysical Journal International*, *200*(1), 596–614. https://doi.org/10.1093/gji/ggu418

Tunini, L., Jiménez-Munt, I., Fernandez, M., Vergés, J., Villaseñor, A., Melchiorre, M., & Afonso, J. C. (2016). Geophysical-petrological model of the crust and upper mantle in the India-Eurasia collision zone. *Tectonics*, *35*(7), 1642–1669. https://doi.org/10.1002/2016TC004161

Vasiukov, D. M., Ismailova, L., Kupenko, I., Cerantola, V., Sinmyo, R., Glazyrin, K., et al. (2018). Sound velocities of skiagite–iron–majorite solid solution to 56 GPa probed by nuclear inelastic scattering. *Physics and Chemistry of Minerals*, *45*(5), 397–404. https://doi.org/10.1007/s00269-017-0928-8

von Seckendorff, V., & O'Neill, H. S. C. (1993). An experimental study of Fe-Mg partitioning between olivine and orthopyroxene at 1173, 1273 and 1423 K and 1.6 GPa. *Contributions to Mineralogy and Petrology*, *113*(2), 196–207. https://doi.org/10.1007/BF00283228

Wang, W., & Wu, Z. (2018). Elasticity of corundum at high pressures and temperatures: Implications for pyrope decomposition and Al-Content effect on elastic properties of Bridgmanite. *Journal of Geophysical Research: Solid Earth*, *123*(2), 1201–1216. https://doi.org/10.1002/2017JB015088

Wang, Z., & Ji, S. (2001). Elasticity of six polycrystalline silicate garnets at pressure up to 3.0 GPa. *American Mineralogist*, *86*(10), 1209–1218. https://doi.org/10.2138/am-2001-1009

Wood, B. J., & Banno, S. (1973). Garnet-orthopyroxene and orthopyroxene-clinopyroxene relationships in simple and complex systems. *Contributions to Mineralogy and Petrology*, *42*(2), 109–124. https://doi.org/10.1007/BF00371501

Woodland, A. B., Angel, R. J., Koch, M., Kunz, M., & Miletich, R. (1999). Equations of state for $Fe_3^{2+}Fe_2^{3+}Si_3O_{12}$ "skiagite" garnet and Fe_2SiO_4-Fe_3O_4 spinel solid solutions. *Journal of Geophysical Research*, *104*(B9), 20049–20058. https://doi.org/10.1029/1999jb900206

Xiong, Z., Liu, X., Shieh, S. R., Wang, F., Wu, X., Hong, X., & Shi, Y. (2015). Equation of state of a synthetic ulvöspinel, $(Fe_{1.94}Ti_{0.03})Ti_{1.00}O_{4.00}$, at ambient temperature. *Physics and Chemistry of Minerals*, *42*(3), 171–177. https://doi.org/10.1007/s00269-014-0704-y

Xu, J., Zhang, D., Fan, D., Downs, R. T., Hu, Y., & Dera, P. K. (2017). Isosymmetric pressure-induced bonding increase changes compression behavior of clinopyroxenes across jadeite-aegirine solid solution in subduction zones. *Journal of Geophysical Research: Solid Earth*, *122*(1), 142–157. https://doi.org/10.1002/2016JB013502

Zhang, L., Ahsbahs, H., Kutoglu, A., & Geiger, C. A. (1999). Single-crystal hydrostatic compression of synthetic pyrope, almandine, spessartine, grossular and andradite garnets at high pressures. *Physics and Chemistry of Minerals*, *27*(1), 52–58. https://doi.org/10.1007/s002690050240

Ziberna, L., Klemme, S., & Nimis, P. (2013). Garnet and spinel in fertile and depleted mantle: Insights from thermodynamic modelling. *Contributions to Mineralogy and Petrology*, *166*(2), 411–421. https://doi.org/10.1007/s00410-013-0882-5

Zunino, A., Khan, A., Cupillard, P., & Mosegaard, K. (2016). Constitution and structure of Earth's mantle: Insights from mineral physics and seismology. *Integrated Imaging of the Earth: Theory and Applications*, 219–243. https://doi.org/10.1002/9781118929063.ch11